NASA/CR–2018–219786

Modeling Issues in Asteroid-Generated Tsunamis

Marsha J. Berger
Courant Institute, New York University, NY

Randall J. LeVeque
HyperNumerics LLC, and *University of Washington, Seattle, WA*

March 2018

NASA STI Program. . . in Profile

Since its founding, NASA has been dedicated to the advancement of aeronautics and space science. The NASA scientific and technical information (STI) program plays a key part in helping NASA maintain this important role.

The NASA STI Program operates under the auspices of the Agency Chief Information Officer. It collects, organizes, provides for archiving, and disseminates NASA's STI. The NASA STI Program provides access to the NASA Aeronautics and Space Database and its public interface, the NASA Technical Report Server, thus providing one of the largest collection of aeronautical and space science STI in the world. Results are published in both non-NASA channels and by NASA in the NASA STI Report Series, which includes the following report types:

- TECHNICAL PUBLICATION. Reports of completed research or a major significant phase of research that present the results of NASA programs and include extensive data or theoretical analysis. Includes compilations of significant scientific and technical data and information deemed to be of continuing reference value. NASA counterpart of peer-reviewed formal professional papers, but having less stringent limitations on manuscript length and extent of graphic presentations.
- TECHNICAL MEMORANDUM. Scientific and technical findings that are preliminary or of specialized interest, e.g., quick release reports, working papers, and bibliographies that contain minimal annotation. Does not contain extensive analysis.
- CONTRACTOR REPORT. Scientific and technical findings by NASA-sponsored contractors and grantees.
- CONFERENCE PUBLICATION. Collected papers from scientific and technical conferences, symposia, seminars, or other meetings sponsored or co-sponsored by NASA.
- SPECIAL PUBLICATION. Scientific, technical, or historical information from NASA programs, projects, and missions, often concerned with subjects having substantial public interest.
- TECHNICAL TRANSLATION. English-language translations of foreign scientific and technical material pertinent to NASA's mission.

Specialized services also include organizing and publishing research results, distributing specialized research announcements and feeds, providing information desk and personal search support, and enabling data exchange services.

For more information about the NASA STI Program, see the following:

- Access the NASA STI program home page at `http://www.sti.nasa.gov`
- E-mail your question to `help@sti.nasa.gov`
- Phone the NASA STI Information Desk at 757-864-9658
- Write to:
  NASA STI Information Desk
  Mail Stop 148
  NASA Langley Research Center
  Hampton, VA 23681-2199

NASA/CR–2018–219786

Modeling Issues in Asteroid-Generated Tsunamis

Marsha J. Berger
Courant Institute, New York University, NY

Randall J. LeVeque
HyperNumerics LLC, and *University of Washington, Seattle, WA*

National Aeronautics and
Space Administration

Ames Research Center
Moffett Field, CA 94035

March 2018

Acknowledgments

This effort was partially supported through a subcontract with Science and Technology Corporation (STC) under NASA Contract NNA10DF26C as part of the Asteroid Threat Assessment Project (ATAP). We would like to thank all participants of this project for many useful discussions, especially Michael Aftosmis, who provided the airburst model, and Darrel Robertson, who provided the ALE3D results. We also thank Jonathan Goodman, Stephane Popinet, Robert Weiss, and Chris Vogl for contributing to this research.

Available from:

NASA STI Program / Mail Stop 148
NASA Langley Research Center
Hampton, VA 23681-2199
Fax: 757-864-6500

Abstract

This report studies tsunamis caused by asteroids, both those that arise from atmospheric blast waves moving across the water surface from airburst asteroids, and those that arise when the asteroid reaches the water and forms a crater. We perform numerical experiments that compare simulations using depth-averaged models (shallow water and several forms of Boussinesq) with linearized Euler (acoustics plus gravity) and ALE hydrocode simulations. We find that neither of the depth-averaged models do a good job of initiating the tsunami, but in some cases can be used to propagate a solution generated by a higher-fidelity method. A list of our conclusions and recommendations for further study is given in Section 5.

Contents

1 Introduction

This report discusses modeling and simulation issues in the generation and propagation of asteroid-generated tsunamis (AGT). We consider both airburst generated tsunamis and those resulting from water impacts. In both these cases, the resulting tsunamis are quite different than earthquake-generated tsunamis (EGT), due to their much shorter wavelength. For EGT simulation, the shallow water equations (SWE) are the method of choice, since they are depth-averaged, removing the vertical direction, and hyperbolic, allowing robust and efficient adaptive solution techniques.

However, as reviewed below, the shallow water equations are derived from the incompressible Euler equations using an asymptotic expansion in powers of h/L, where h is the depth of the ocean, and L is the wavelength of the phenomena. For earthquakes L can be $O(100)$ km. For airbursts, a typical length scale of a Friedlander blast profile is $O(10)$ km. For craters caused by an asteroid splashing into the water, the diameter may be only 1–3 km, calling into question the suitability of the SWE to model these events.

In this report we compare SWE simulations with both linearized Euler equation results and with several forms of Boussinesq equation simulations, to determine numerically how reliable the simulations are. There are several forms of Boussinesq equations, but roughly speaking they include the next terms in the asymptotic expansion used to derive the shallow water equations. We use a model problem to compare all three equation sets to demonstrate their behavior, and when they can be used reliably. Finally, we also take data from a hydrocode simulation to determine whether it can be propagated using the Boussinesq equations.

Section 2 briefly introduces the models we compare, with more details about them given in the Appendix. We also introduce the problems we study and the computer codes used. Section 3 looks at airburst-generated tsunamis, the simpler of the two scenarios. Section 4 looks at water impact cases. This is not as far along, but we present a number of experiments to justify our conclusions and recommendations, found in Section 5. We end with a list of questions not yet answered and recommendations for further study.

2 Fluid Dynamics Models

2.1 Model equations

In this report we focus on models for the generation and propagation of the tsunami wave in the water, its interaction with underwater topography (bathymetry) and the resulting inundation onshore. We do not discuss models for asteroid propagation through the atmosphere, the energy deposition from an airburst, or the physics of an asteroid striking the ocean and forming a crater.

Even so, there are many possible tsunami models:

- **3D compressible or incompressible Navier-Stokes equations with a free surface.** This would be the most accurate model but is impractical for oceanic scale computations and generally not necessary. Neglecting fluid viscosity gives the simpler 3D compressible Euler equations but still not practical. Multi-physics codes might reduce to these equations in the fluid phase, and be necessary for modeling asteroid impact cratering, but we do not consider these equations for our study of tsunami propagation. A simplification is a 2D vertical slice in (r, z) with source terms to model radial symmetry. Simulations with the hydrocode ALE3D [1] that models these equations have been performed by Darrel Robertson and used to initialize crater-generated tsunamis in Section 4.

- **3D linearized compressible Euler.** When the surface displacement is small relative to the depth (e.g. for airburst generated tsunamis), the free surface can be replaced by a boundary condition at the top of the water and the nonlinear compressible Euler equations linearized about the equilibrium state. This gives the linear acoustics equations, with the addition of a gravity term and appropriate boundary conditions at the top surface to model the atmospheric pressure and water surface displacement. We refer to this set of equations as **3D AG** (acoustics plus gravity).

  In the depth-averaged shallow water equations, the variables are the depth $h(x, y, t)$ and two horizontal momenta hu and hv. There is no need for a free surface or a boundary condition at the top since the depth h directly models the surface displacement by $\eta(x, y, t) = B(x, y) + h(x, y, t)$, where $B(x, y)$ is the bathymetry (relative to mean sea level, say, with $B < 0$ in the ocean and $h \geq 0$).

- **2D shallow water equations.** These equations are derived from the 3D incompressible Euler equations by assuming that the wavelength of the surface disturbance is long compared to the fluid depth. These equations are often used for modeling earthquake generated tsunamis, for which the wavelength may be hundreds of kilometers while ocean depth is 4 km on average. The nonlinear shallow water equations have also been shown to be a good model for inundation in many cases.

- **2D Boussinesq equations.** The shallow water equations are *non-dispersive*; a small amplitude wave propagates at the gravity wave speed $\sqrt{gh}$ regardless of its wavelength. This is roughly correct for wavelengths that are large relative to the fluid depth, but for wavelengths less than say 20 times the fluid depth, the propagation speed predicted from the linear Euler equation theory begins to depend strongly on wavelength, with shorter wavelengths traveling more slowly. Asteroid-generated tsunamis have wavelengths that are much smaller than those generated by major earthquakes, and so the shallow water equations are generally inadequate to model their propagation.

  The dispersive effect can be modeled with depth-averaged equations if additional terms are kept when deriving these from the Euler equations. This introduces higher-order derivatives in the equations, making them more expensive to solve numerically, but still much cheaper than solving full 3D equations.

There are many such *Boussinesq equations* depending on how the expansion is done and/or how the higher order terms are modified to better match the dispersion relation of the Euler equations. We use a form described in Section A.4. These equations match the dispersion relation well down to wavelengths of about 2 times the fluid depth, see Figure A1.

- **Plane-wave or radial versions**: All the models above can be simplified when modeling a radially symmetric wave by incorporating appropriate geometric source terms in the equations. The 3D versions of AG reduce to 2D computational work, and the 2D versions reduce to 1D, allowing for computationally efficient parameters studies, for example.

2.2 Computer codes

Simulations using these models were performed using a variety of codes. All AG simulations used Clawpack with adaptive mesh refinement in the x-z plane where z is depth, or in the r-z plane with the inclusion of geometric source terms to model radial symmetry, so that the horizontal direction is radius from the impact location.

The 2D shallow water simulations were performed using GeoClaw, for both flat bottom experiments and real topography [2]. One-dimensional shallow water equations (with or without radial source terms) were also performed using a newly-developed 1D extension of GeoClaw.

We tested several different Boussinesq codes that use different formulations of the equations, mentioned in the text in the relevant places. In particular BoussClaw refers to an extension of GeoClaw initially developed by Jihwan Kim that implements the equations studied by Madsen and Sorensen [3]. This formulation has a parameter $\mathcal{B}$ that can be set to $\mathcal{B} = 0$ to solve the Peregrine equations [4], an early version of Boussinesq equations that is generally too dispersive. The choice $\mathcal{B} = 1/15$ is recommended as giving the best agreement with the dispersion relation expected from the Euler equations, and we have also found that this works very well. Details can be found in Section A.4.2 and in the papers [3, 5–7].

The other computer code used for some Boussinesq simulations is Basilisk (courtesy of Stephane Popinet), which solves the Serre-Green-Naghdi equations (SGN) [8]. The Basilisk code is parallelized. It is also adaptive, but not flexible or robust enough to handle the cases we consider, so adaptivity is not used in the results below. The SGN implementation in Basilisk was found to agree fairly well with BoussClaw with $\mathcal{B} = 1/15$. Both Boussinesq codes are used in the experiments below to help confirm the numerical results.

The ALE simulations performed by Darrel Robertson were done using the hydrocode ALE3D [1]. This is a multi-physics arbitrary Lagrangian-Eulerian code that includes heat transfer, multiphase flow, fracture and fragmentation models, radiation, etc. It is very computationally expensive, providing motivation to investigate whether depth-averaged codes can propagate asteroid-generated tsunamis and if so, how early in the process can this be done.

2.3 Initial conditions

As inputs to generate a tsunami we consider the following possibilities:

- An airburst results in a pressure pulse that hits the water surface and spreads out, moving over the surface at roughly the speed of sound in air. This pressure pulse typically has the form of a shock wave (with an overpressure that depends on the size and material properties of the asteroid) that decays with distance from the initial impact, followed by a rarefaction wave that reduces the pressure below atmospheric pressure before returning to equilibrium. The idealized *Friedlander profile* is shown in Figure 1. This modified atmospheric pressure acts as a forcing term on the water surface, deforming the surface and creating a tsunami.

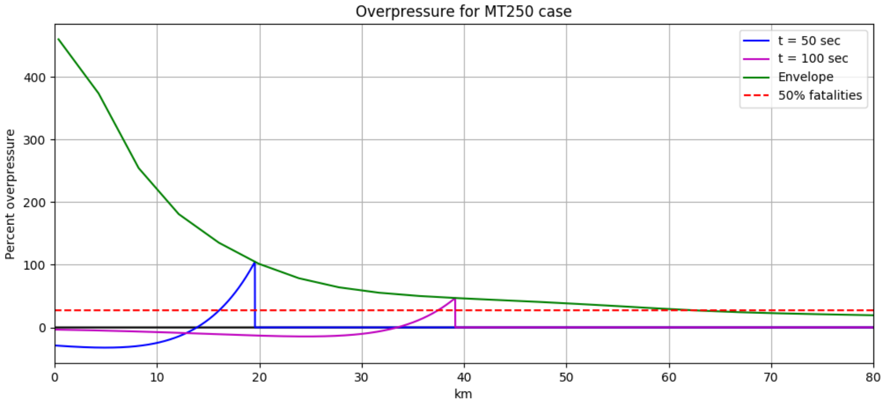

Figure 1. Friedlander profile: the atmospheric pressure pulse from an airburst blast wave.

- An idealized crater can be used directly as initial data for a tsunami model (e.g. the parabolic crater shown in Figure 2 with zero initial fluid velocity, discussed in several papers [9,10]). Although a crude model of reality, a tsunami model with this initial data is much cheaper to run than the multi-physics code, and so it is useful to investigate whether such simulations can be used as a reasonable estimate of tsunami magnitude provided they are properly calibrated. It also simplifies comparisons of propagation using hydrocodes and tsunami codes without the additional complicating physics.

- An asteroid that reaches the water surface forms a crater that may be quite deep, or even reach to the sea floor. Properly modeling the crater formation (including drastic temperature changes and vaporization of some of the water, vertical acceleration of the fluid, transfer of momentum from the asteroid to the fluid, etc.) requires multi-fluid and multi-physics codes and the initial phases of crater generation and evolution cannot be well modeled by a tsunami code alone. (For now we are ignoring the air blast that accompanies the cavity since it moves on a faster time scale). But output from an impact code at a later time, after the initial tsunami generation, can potentially be used as initial conditions for a tsunami model to accurately model the long-distance propagation and onshore inundation of the wave.

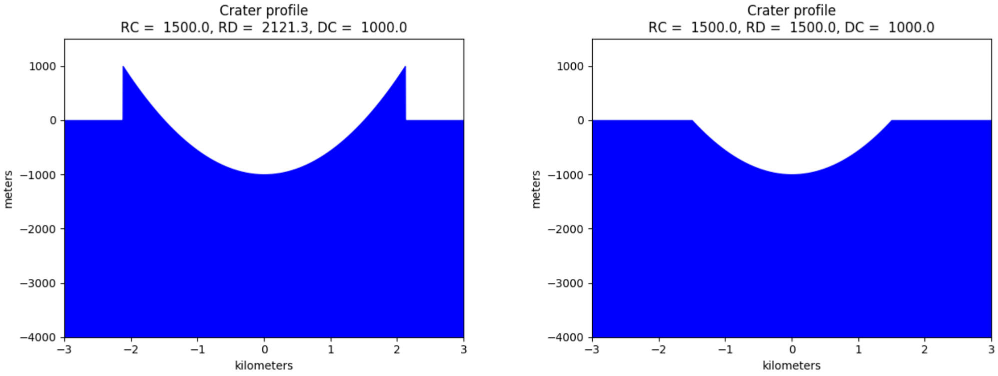

Crater profile
RC = 1500.0, RD = 2121.3, DC = 1000.0

Crater profile
RC = 1500.0, RD = 1500.0, DC = 1000.0

Figure 2. Parabolic crater, with and without lip. The surface elevation is nonzero only for $r < RD$, where $\eta(r) = -DC(1-(r/RC)^2)$. Here the depth of the crater is $DC = 1000$, the radius is $RC = 1500$ and RD is either $RD = \sqrt{2}RC$ for the lip case or $RD = RC$ for no lip.

3 Airburst-generated tsunamis

The pressure pulse arising from an airburst hits the water and then moves across it, causing two distinct waves: The *response wave*, a disturbance of the sea surface that is directly coupled to the moving pressure pulse and that propagates at the same speed (roughly the speed of sound in air, $s_a \approx 391.5$ m/sec), and a *gravity wave* that is generated from the pressure growing at the initial point of impact and that moves at slower speeds bounded above by $s_g = \sqrt{gh}$ (slower for higher wave numbers when dispersion is included). Here h is the undisturbed depth which we assume is constant for this initial discussion. If $h = 4000$ m then $s_g \approx 200$ m/sec, and for all oceans on earth we have $s_g < s_a$.

In this section we discuss the ability of the three broad classes of models (SWE, SGN/BoussClaw and AG) both to generate and to propagate across long distances the response wave and the gravity wave. We note that even for Boussinesq equations, shoreline inundation is often modeled by switching to the shallow water model. In very shallow water the wavelengths become more appropriate for this model and eventually the waves break, which is modeled better by the shocks that form in the nonlinear shallow water equations than by the Boussinesq equations. In addition, the larger stencils of Boussinesq models are much more difficult to use at the wet/dry interface and the higher-order derivatives arising in this model are not well defined or justified.

The air blast model used in this study was provided by Michael Aftosmis. It simulates the pressure disturbance at sea level resulting from a 250MT airburst at 10 km. altitude. For details of how the airburst was computed see [11].

3.1 Response wave

The overpressure of the blast wave pressing down on the sea surface might be expected to cause a depression, and this would be the form of the response wave if $s_a < s_g$. But since the pressure pulse moves faster than the gravity wave speed, it turns out that the response wave has positive amplitude where the overpressure is positive. This is seen in all three models as well as in simulations using several hydrocodes.

For a traveling plane wave solution of the linearized shallow water equations it can be shown (see [12]) that a propagating atmospheric pressure pulse $p_{atm}(x, t)$ induces a response wave that has the same shape, with an amplitude (sea surface deformation) given by:

$$\eta(x,t) = \frac{h_0\, p_{atm}(x,t)}{\rho_w(s_a^2 - s_g^2)}. \tag{1}$$

Here h_0 is the undisturbed ocean depth, and $\rho_w = 1025$ kg/m^3 is the density of sea water. The same holds true approximately for a radially expanding pressure pulse p_{atm} for large r.

Note that the amplitude (1) varies approximately linearly with ocean depth (not exactly since $s_g^2 = gh_0$). For AG, we do not have a simple formula, but the response is very similar but with smaller amplitude. The difference is smaller when the water is more shallow, since then SWE are a better model of the AG behavior. The sharp discontinuity seen in the Friedlander profile $p_{atm}(r, t)$ of Figure 1 also smoothes out when the dispersive AG equations are used, as can be observed in Figures 4 and 5.

Figure 3 shows the amplitude of the shallow water response wave as a function of ocean depth when $p_{atm} = 1$ atmosphere. The amplitude varies roughly linearly with depth of the ocean, going up to about 3.5 m at 4000 m depth. (Initially, around the peak of the airburst in Fig. 1, which has an overpressure of 4.5 atm, the response wave amplitude is over 17 m.) If p_{atm} is reduced, then this plot scales linearly. At the pressure 0.273 atm at which 50% fatality is expected from the blast itself, the amplitude of the response wave would be roughly 1 m at 4000 m depth.

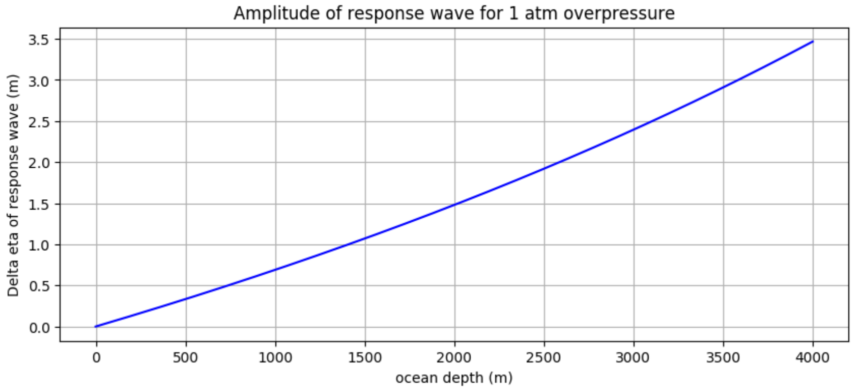

Figure 3. Response wave amplitude $\Delta\eta$ when $p_{atm} = 1$ atm overpressure, as a function of ocean depth, using the shallow water equations.

As the atmospheric pressure disturbance propagates into shallower water the amplitude of the response wave decreases and vanishes at the shoreline. However, some of the energy of the response wave is converted into a gravity wave as the blast wave propagates over varying topography and so there is some inundation expected from the response wave itself, but in numerical experiments this has always been very small. This is seen for example at time $t = 240$ seconds in the surface displacement plots at a distance of around 78 km in Figure 8 below. There is a gravity wave generated as the response wave hits the shelf, but it is also quite small compared to the main gravity wave. In the horizontal velocity plots, the response wave is visible at about $x = 93$ km, but is barely visible in the surface displacement.

For these reasons we believe the response wave itself will not cause any dangerous flooding provided the blast is sufficiently far offshore that people near the shore survive the blast wave itself.

3.2 Gravity wave

The initial impact of the blast wave and its outward spread does cause a depression on the ocean surface that gives rise to a more slowly moving gravity wave. We now consider the possibility that this tsunami wave can cause dangerous flooding.

In order to properly model the initial generation of the gravity wave, we have found it necessary to use the acoustics+gravity (AG) equations in order to capture the vertical variations within the ocean depth during this initial generation phase. Figures 4 and 5 show some frames from a simulation over the first 100 seconds of a simulation using the AG equations with a flat 4000 m deep ocean floor. The 250 MT Friedlander blast wave from Figure 1 is used as a forcing term at the top surface.

Note the following in Figures 4 and 5:

- The surface pressure plots (left side, top plots) show the pressure at the top surface in the water. curve. The black dashed curve shows the Friedlander profile, the imposed atmospheric pressure, and the red curve is the water surface pressure including the $\rho_w g \eta$ term.
- Lower left plots show the r-z computational plane where r is radial distance and z is the depth of the ocean. The pressure is shown as a Schlieren plot over the depth of the ocean, in which gradients of pressure are plotted on a logarithmic scale. This clearly shows very small amplitude pressure waves propagating at the speed of sound in water that would not show up in a pseudocolor plot.
- The speed of sound in water is set to 1500 m/sec. Note that it takes nearly 3 seconds for the pressure pulse to reach the sea floor.
- The horizontal velocity is plotted in the r-z plane and shows that initially this is far from constant through the depth, while at later times it becomes more so, e.g. by time 30 seconds in Figure 5, at least for the longer wavelength waves.

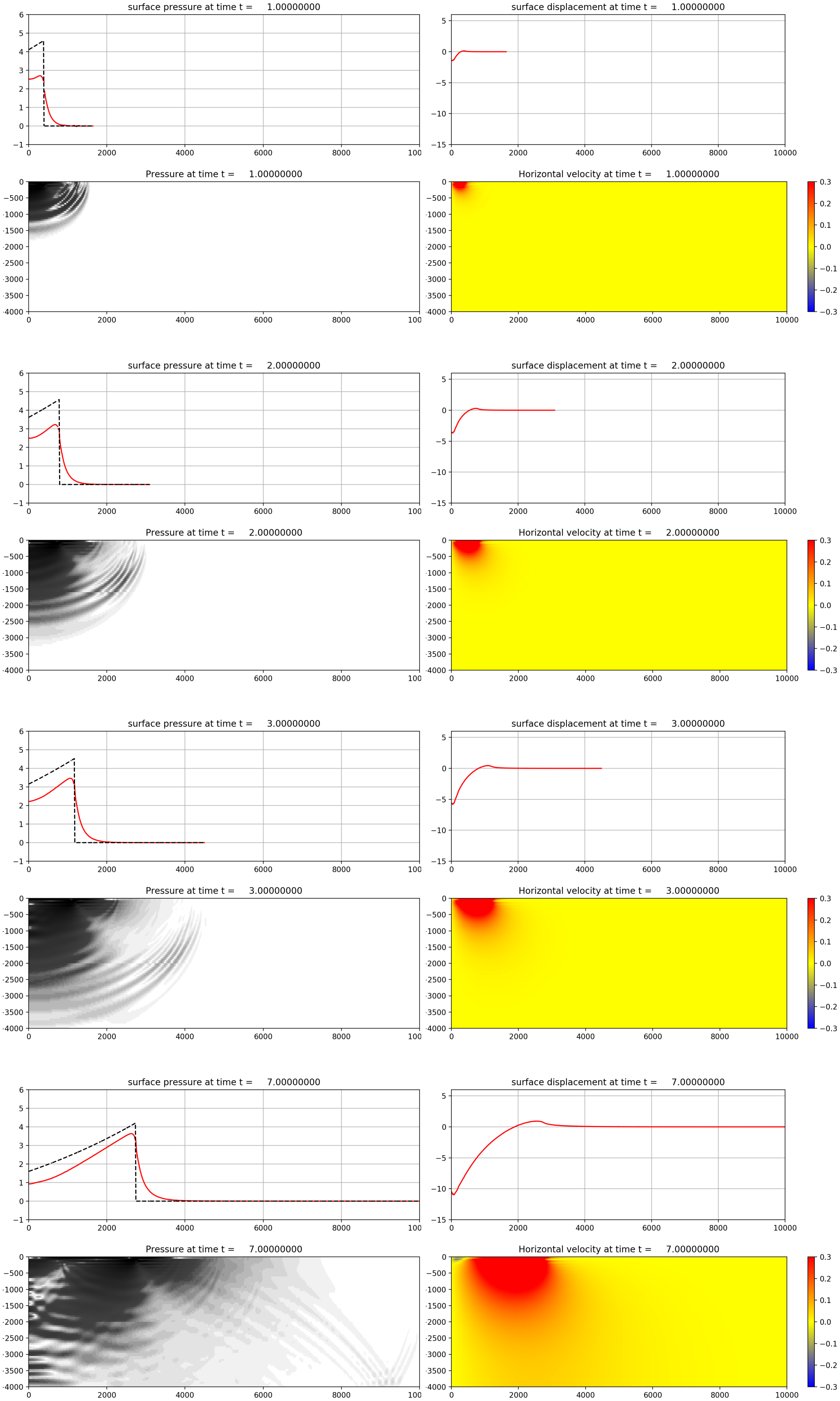

Figure 4. Initial generation of airburst tsunami using AG model with radial symmetry. Selected frames over first 7 seconds, over a radial distance of 10 km. In top plots, red curves are surface traces of solution, black dashed line is atmospheric pressure (Friedlander profile).

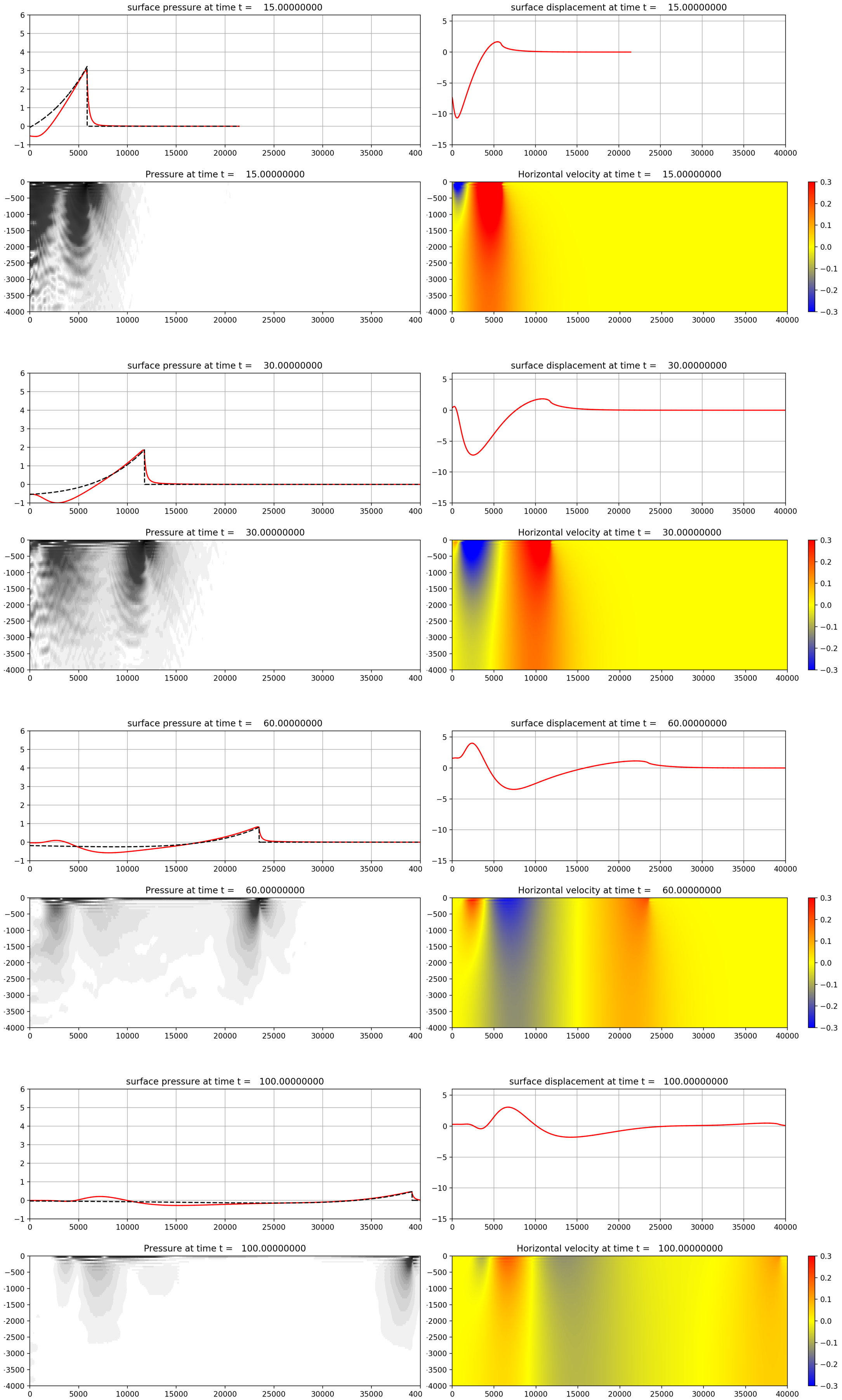

Figure 5. Initial generation of airburst tsunami using AG model with radial symmetry. Selected frames over first 100 seconds, over a radial distance of 40 km. In top plots, red curves are surface traces of solution, black dashed line is atmospheric pressure (Friedlander profile).

3.2.1 Depth-averaged simulations: *ab initio* tests

We experimented extensively using the depth-averaged shallow water equations with the inclusion of a source term modeling the atmospheric pressure of the blast wave. We found that these equations could model the propagation of the response wave that is coupled to the blast quite well, and indeed it can be shown analytically that there are traveling wave solutions to the linearized SWE that match the nonlinear response wave (1) quite well. However, the gravity wave generated using this approach is only reasonable if the water depth is small. Since the positive pressure pulse is only about 10 km long (see Figure 1), in deep water we expect the generation of dispersive waves, as seen in the AG simulations, and these are absent when SWE are used.

We also tested using the same source term from SWE in the Boussinesq equations, but did not get good agreement with the AG results. It was suggested to us[1] that we modify the pressure forcing to incorporate more terms using the same asymptotic expansion used to derive the Boussinesq equations themselves, but we have not yet had time to incorporate this. Finally, the r-z plane plots in Figures 4 and 5 show that in the initial phase of tsunami generation there are significant vertical variations that probably cannot be captured with depth-averaged equations.

Figure 6 shows snapshots of the all the models we considered with the same airburst pressure forcing, in a 4 km deep ocean. This includes the shallow water equations (in 2D), the SGN equations (in 2D), BoussClaw (using the 1D radial version), and the AG solution (again using the 1D radial code). The response waves match well, though they have different amplitudes, but the gravity waves are completely different, both quantitatively and qualitatively. Note that:

- The shallow water model generates a deep depression with almost no waves with positive amplitude.
- The AG and the Boussinesq models agree quite well, after 200 seconds, in tracking the first wave, and by 400 seconds in several of the leading waves.
- The Boussinesq codes generate larger gravity waves than the AG simulations. The largest of them are not the leading waves, and are not present in the AG simulation.
- All codes have much closer agreement with the forced response wave then they do with the gravity waves that are generated.

For comparison purposes in Figure 7 we also include here some snapshots of the same codes but in a 1 km deep ocean. The waves move more slowly in the shallower water, so the snapshots are every 100 seconds for 400 seconds. In shallower water we expect a closer match between the models. The Boussinesq codes start agreeing with the AG simulation at an earlier time than in the deeper ocean. Note that the scale on the axes is not the same as in the previous figure; the wave amplitude is smaller than in the 4 km deep ocean.

---

[1] Thanks to Jonathan Goodman for this suggestion. He has derived the next terms in a modified pressure forcing in one space dimension.

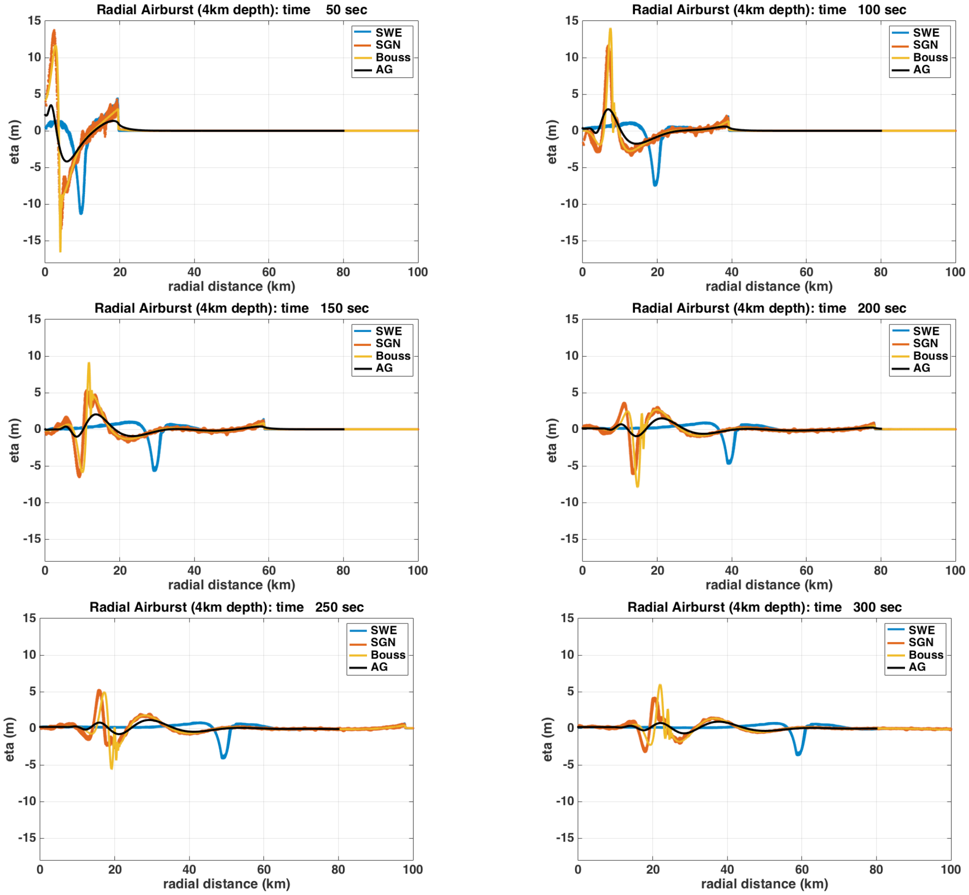

Figure 6. Comparison of initial generation of airburst tsunami using all 4 models in a 4 km deep ocean. Selected frames every 50 seconds. After 300 seconds, SGN and BoussClaw match AG in the leading gravity wave, but not (yet) the rest. The SWE model does not generate gravity waves that match AG at any of the times.

We have shown here that the depth-averaged models do not generate a realistic gravity wave from the pressure forcing. Once the gravity wave is established however, there is a better chance of accurately modeling its propagation using depth-averaged equations. In Section 3.2.3 we turn to experiments that show that using a suitable Boussinesq equation with initial conditions coming from the AG simulation can be successful.

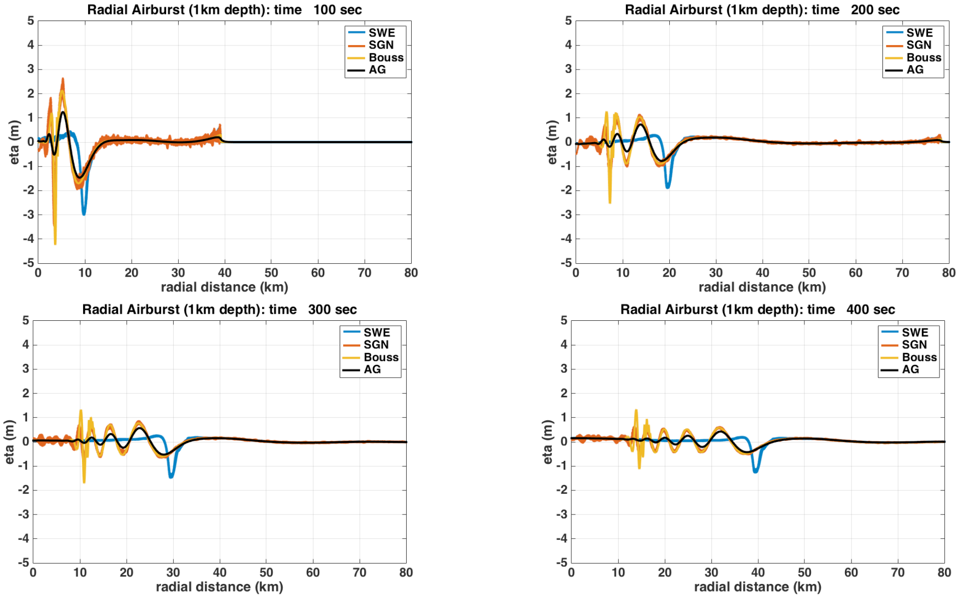

Figure 7. Comparison of airburst generated tsunamis using all 4 models in a 1 km deep ocean. Selected frames every 100 seconds. After about 200 seconds, SGN and BoussClaw match AG in the leading gravity wave, and by 400 seconds, the next few waves are very similar, though the amplitude is not quite right. The shallow water model still has very different waves.

3.2.2 AG simulation with continental shelf

In this section we explore what happens when the ocean waves hit a continental shelf. The above experiments showed the initial phase of tsunami generation on a flat ocean bottom at 4 km depth. When the response wave encounters variable topography, new gravity waves can be generated.

The left column of Figure 8 shows later times from a radially symmetric AG simulation where waves move up a slope onto a continental shelf with a water depth of 200 m. (The right column shows a comparison with a Boussinesq solution, discussed below in Section 3.2.3.)

Note the following:

- At time 180 seconds, the atmospheric blast wave has propagated to 70.47 km and is starting to move up the shelf slope. The dispersive gravity wave is moving much more slowly.
- At time 240 seconds, the atmospheric blast wave has propagated to 93.96 km and is visible in the horizontal velocity plot, but barely visible in the surface displacement. Recall that the amplitude of the response wave given by (1) is smaller in shallow water, since it is proportional to the depth.
- At time 240 seconds one can see an additional surface displacement at roughly

75 km, the start of the continental shelf. This is a gravity wave that is generated by the interaction of the response wave with the varying topography.

- At time 500 seconds, the waves on the shelf arose from the response wave interacting with the shelf slope. The first big wave from the gravity wave train is moving up the slope at this time.
- At time 900 seconds, the first 4 waves from the dispersive wave train have moved onto the shelf, where they are compressed and move more slowly. Note from the plot of horizontal velocity that the velocity is amplified more strongly. The shoaling of these waves appears to be very well modeled with the Boussinesq equations used here, as discussed further in Section A.4.2.

3.2.3 Depth-averaged simulations: Initialized from AG

The right column of Figure 8 shows results obtained using the Boussinesq equations with parameter $\mathcal{B} = 1/15$. This simulation was initialized with data coming from the AG simulation discussed above at time 180 seconds. This was chosen to be large enough that the response wave is well separated from the gravity wave. The response wave was then zeroed out by smoothing the surface η to zero to the right of 40 km. The horizontal velocity from the AG simulation was depth-averaged to provide initial data for the velocity in the Boussclaw simulation.

Note the following:

- The blue curves in the right column of Figure 8 show the Boussinesq solution, the red curves are from the original AG simulation (and depth averaged for the velocity component). At $t = 180$ seconds they agree exactly to the left of 40 km, to the right the response wave has been suppressed.
- At later times the response wave generates a gravity wave when it interacts with the shelf that is not captured by the Boussinesq solution, but the gravity wave originally generated at the origin is well modeled, both during its propagation on the flat bottom and as it transitions onto the shelf.
- There are other forms of the Boussinesq equation that we have tried and that do not work as well. The left column of Figure 9 shows the comparison to AG when the Peregrine model (see Section A.4.1) is used for the same experiment. The non-dispersive shallow water equations also do not work well for this problem, as seen in the right column of Figure 9.

We conclude that even as the waves shoal on the continental shelf, the Boussinesq model can be used for propagation, as long as they are initialized with an appropriate transfer of data from a model that is better at generating the waves from an airburst. This is consistent with the fact that the airburst-generated tsunami has a wavelength of around 10 km, a factor of 2.5 greater than the ocean depth, and the Boussinesq equations with $\mathcal{B} = 1/15$ do a good job of modeling the dispersion and shoaling properties down to a wavelength/depth ratio of around this magnitude, as seen in the plots of Figure A1. The SWE equations, on the other hand, only agree well for much larger ratios as can also be seen from these plots.

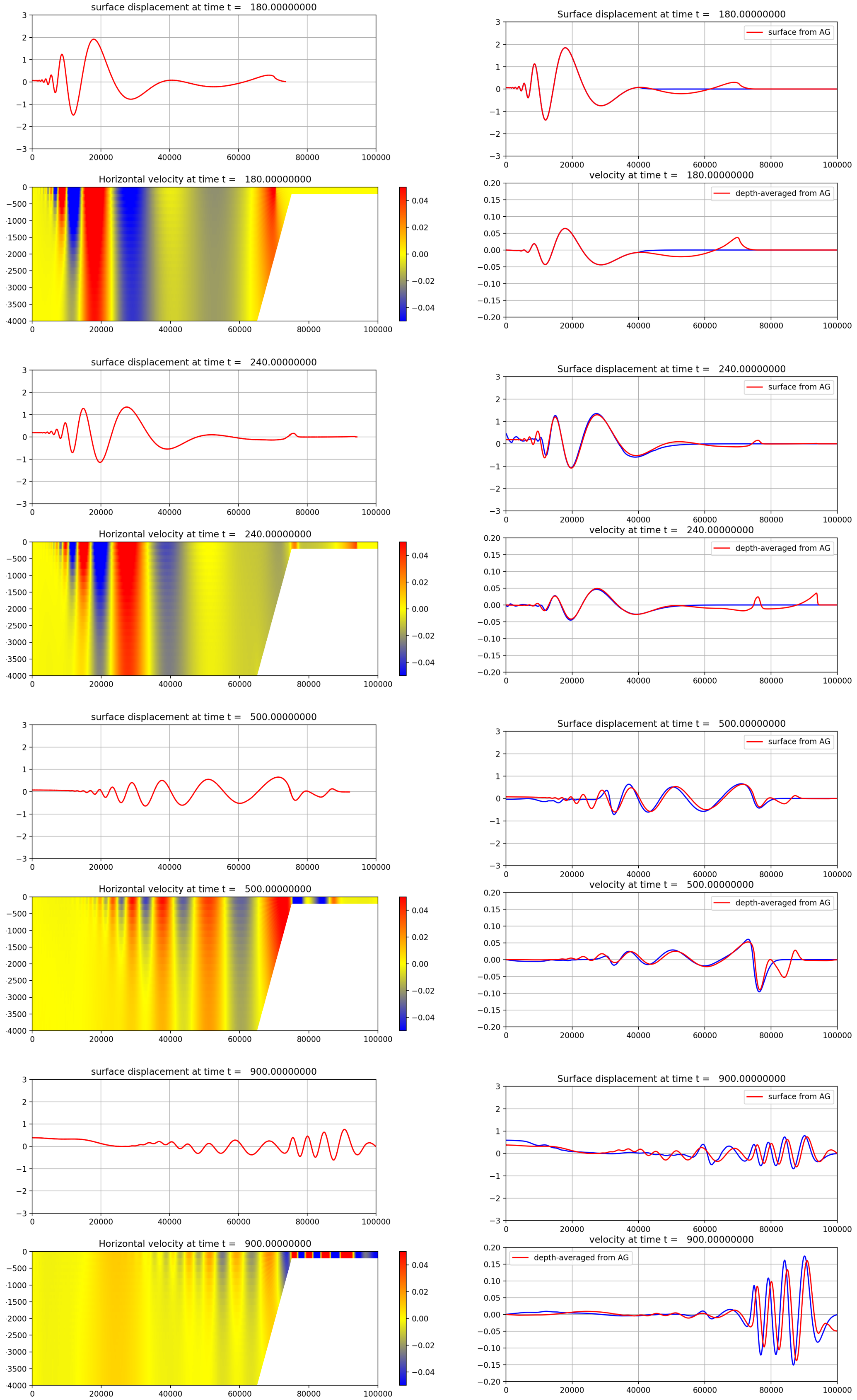

Figure 8. The left column shows selected frames of the AG simulation of an airburst tsunami generated in 4000 m ocean and moving onto a continental shelf of depth 200 m. The right column shows the AG results in red and simulations obtained with the Boussinesq depth-averaged equations in blue, when initialized with the AG gravity wave at 180 seconds (suppressing the response wave).

Figure 9. The left column shows in blue the solution to the Boussinesq equations with parameter $\mathcal{B} = 0$, the Peregrine model. This is too dispersive relative to the AG solution (red curve). The right column shows in blue the solution to the non-dispersive shallow water equations with the same initial data, compared to the AG solution (red).

3.3 Depth-averaged simulations and parameter study

Since the acoustics plus gravity model is much more computationally intensive than depth-averaged models, one would hope to use the latter in a parameter study with varying shelf length and slope, distance from blast, and ocean depth. Here we show some initial results from the start of this effort. This study uses the 1D version of the models with radial source terms, so both the bathymetry and the airburst forcing is radially symmetric.

The parameters that we can vary are the length of the deep ocean, the length of the continental slope, the depth and length of the continental shelf, and the slope of the beach. The parameters are illustrated in Figure 10.

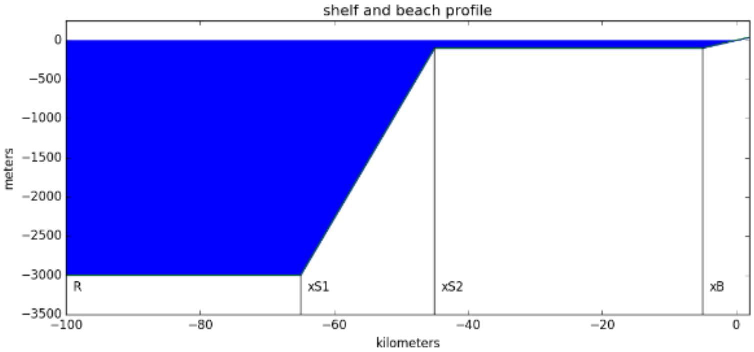

Figure 10. Illustration of idealized radial bathymetry used for the parameter study with the indicated variables.

We initialize either SWE and BoussClaw with data taken from an AG simulation at 180 seconds. The experiments shown in the previous section illustrate that starting with this data and propagating further with the Boussinesq equations gives good agreement with the AG results at later times. Propagating further with SWE did not agree well, but since SWE is much cheaper to solve in 2D than Boussinesq, we are interested in seeing how SWE results compare to the more correct Boussinesq results. The surface displacement is transferred from the AG run to the depth-averaged equations, and the velocity is initialized so that it corresponds to an outward propagating wave.

Figure 11 shows the initial data used for the parameter study on the left, for one particular choice of topography. The plot on the right shows the solution at a later time using the Boussinesq equations. At this time the dispersive wave generated in the deep ocean is shoaling and the portion that has passed onto the shelf already has increased amplitude. The red curve shows the maximum gravity wave height that was calculated at each point over the entire computation. From this you can see that the amplitude decays as the wave propagates over the deep ocean (partly because of radial spreading, and partly because the main peak loses amplitude as dispersive waves fall behind).

In Figure 12(a), we show results from the parameter study, in the form of a plot of the maximum runup observed on a beach as a function of the total distance from the initial airburst to the shore. The '×' symbols show results computed using SWE

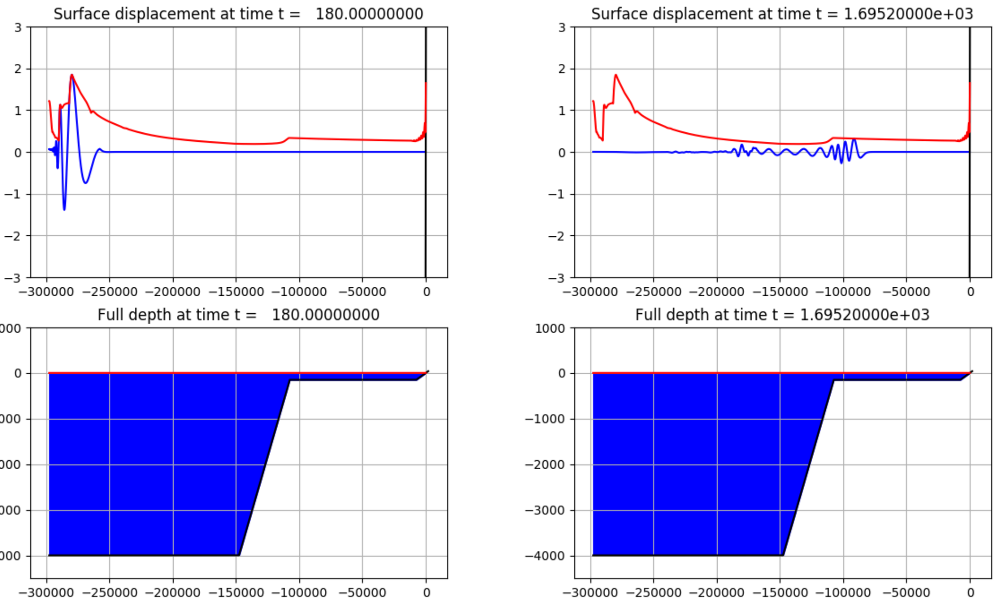

Figure 11. Left: Initial data at time $t = 180$ used for all cases in the parameter study. Right: Solution to the Boussinesq equations at a later time as the wave is shoaling. The red curves shows the maximum amplitude of the wave over all time.

and the '•' are from BoussClaw. All simulations use a 4 km deep ocean and a 150 m deep shelf. The length of the continental slope is 40 km, and the beach slope is 0.02, near the lower lower limit for broad sloping beaches. The beach extends a distance of 7.5 km from the shore to a depth of 150 m. The only parameters varied are the length of the shelf and the length of the deep ocean between the source location and the start of the continental slope. The shelf length varied from 0 to 150 km and the length of the deep ocean varied between 50 and 150 km. A deep ocean length of at least 50 km was used since the initial data at $T_0 = 180$ seconds has a wave train that has expanded out to slightly more than 40 km.

Multiple points at the same horizontal point in Figure 12(a) correspond to different combinations of deep length and shelf length that give the same total distance.

Both the SWE and Boussinesq equations yield runup curves that vary smoothly with distance, providing hope that a reasonable engineering model could be derived. Note that all results are bounded above by the SWE zero shelf length case. The runup decreases with distance from the beach with both equation sets, but more so in Boussinesq, where presumably there is more time for the waves to disperse and decay in the deeper water.

Also note the interesting fact that for a given total distance, the runup observed with Boussinesq tends to increase as the shelf becomes longer (and the deep ocean length correspondingly shorter), whereas the opposite trend is observed from the shallow water results. Examining movies of these simulations reveals the following. With the shallow water equation, the initial data decays slowly over the deep ocean due to radial spreading, but remains coherent with one dominant peak since these

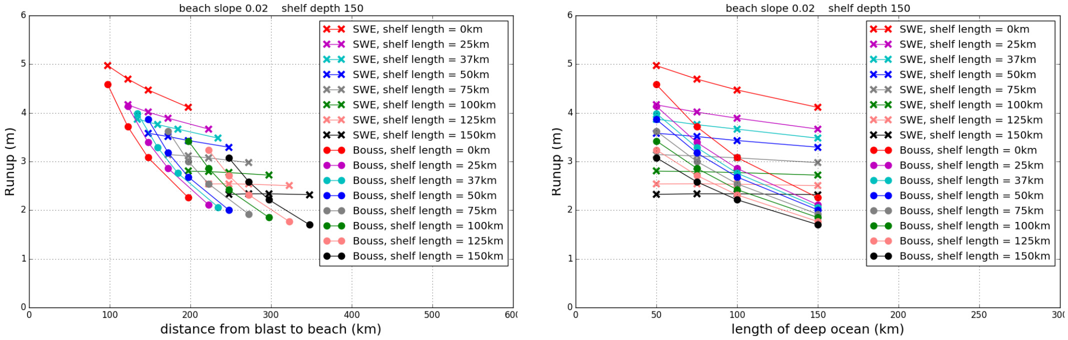

Figure 12. Parameter study comparing SWE and BoussClaw (1D with radial source terms, $\mathcal{B} = 1/15$) in a study of shoreline runup. The solution is initialized from an AG simulation before the waves hit the continental slope. 'X' is a shallow water solution, and '•' is a BoussClaw solution.

equations are non-dispersive. This is seen clearly in Figure 12(b) where the results are plotted relative to the length of the deep ocean segment alone. The SWE results show that the eventual runup is almost independent of the deep ocean length, especially for the longer shelf lengths. As the SWE wave moves into shallower water on the shelf there is initally significant amplification due to shoaling, followed by decay on the shelf. If the shelf is long enough, then nonlinearity on the shallow shelf comes into play and the shallow water wave can steepen into a shock (the van Dorn effect, e.g. [13]), which decays much faster than it would from radial spreading alone. So the longer the shelf, the more decay and hence smaller runup.

For Boussinesq, on the other hand, the dispersion causes much faster decay of the main wave in the deep ocean, due to energy being shed into additional oscillations behind. On the shelf there is very little decay due to dispersion since the wavelengths are now much longer relative to the fluid depth. Also, with the dispersive equations the wave does not steepen into a shock and so there is no extra decay from this effect. We can see in Figure 12(b) that increasing the length of the deep ocean leads to decay in the Boussinesq runup and also that when this length is fixed, increasing the shelf length causes further decay (the curves shift downward) but not by as much as the SWE curves. The combination of faster decay in the deep ocean and slower decay on the shelf leads to the different ordering of the curves in Figure 12(a) relative to the SWE results.

Figures 13 and 14 show a few frames from two cases of the parameter study to illustrate the discussion above.

These radially symmetric tests are perhaps of limited predictive value since on real topography the geometry of the shelf can lead to areas of focusing or defocusing and the shore topography is rarely a smooth sloping beach. But we hope that they provide some guidance on the manner in which runup decreases with increasing distance of an airburst offshore. They also suggest that simulations performed with shallow water equations may be sufficient to obtain an upper bound on the runup that would be computed with the more expensive Boussinesq equations.

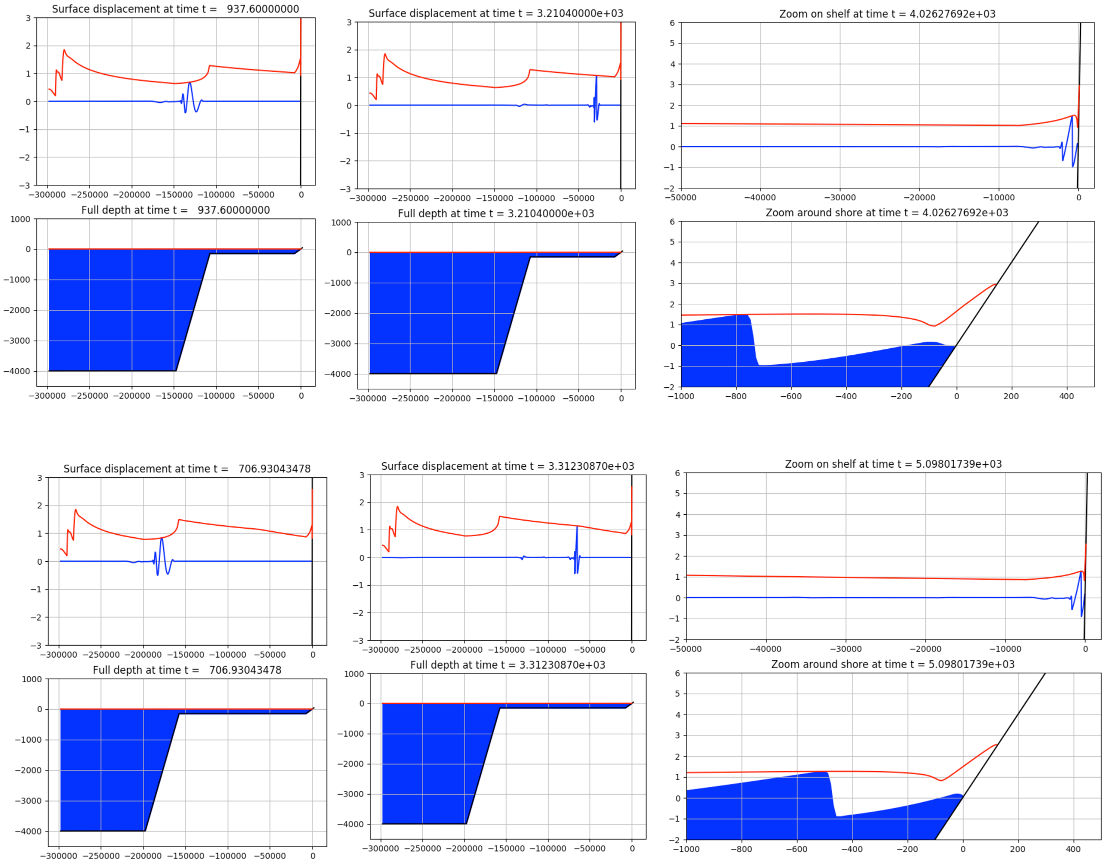

Figure 13. Frames from parameter study using the shallow water equations. The top row shows three frames from the case where the deep ocean is 150 km long and the shelf is 100 km long. The bottom row shows the case where the deep ocean is 100 km long and the shelf is 150 km long. In each case the first frame is as the wave is shoaling, the second frame is as it is propagating on the shelf, and the third frame shows a zoom of the wave approaching the beach. Note the shock formation on the shelf. The red curves are the maximum amplitude of the solution over the full length of the computation, while blue curves (filled or unfilled) show the solution at specific times.

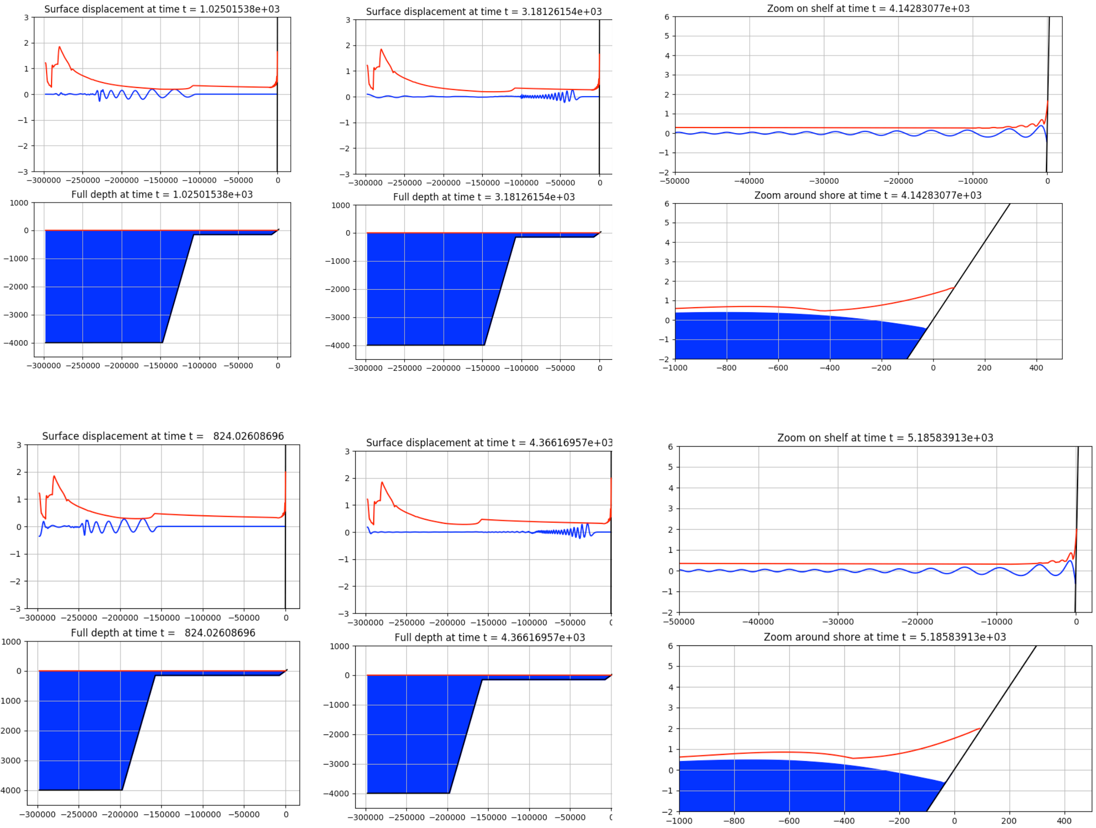
Surface displacement at time t = 1.02501538e+03

Surface displacement at time t = 3.18126154e+03

Zoom on shelf at time t = 4.14283077e+03

Full depth at time t = 1.02501538e+03

Full depth at time t = 3.18126154e+03

Zoom around shore at time t = 4.14283077e+03

Surface displacement at time t = 824.02608696

Surface displacement at time t = 4.36616957e+03

Zoom on shelf at time t = 5.18583913e+03

Full depth at time t = 824.02608696

Full depth at time t = 4.36616957e+03

Zoom around shore at time t = 5.18583913e+03

Figure 14. Frames from parameter study using the Boussinesq equations. The top row shows three frames from the case where the deep ocean is 150 km long and the shelf is 100 km long. The bottom row shows the case where the deep ocean is 100 km long and the shelf is 150 km long (the same cases as shown in Figure 13. In each case the first frame is as the wave is shoaling, the second frame is as it is propagating on the shelf, and the third frame shows a zoom of the wave approaching the beach. Note the Boussinesq wave decays most rapidly on the deep ocean. The red curves are the maximum amplitude of the solution over the full length of the computation, while blue curves (filled or unfilled) show the solution at specific times.

3.4 Propagation and inundation on real topography

In this section we use the radially-symmetric wave form from the AG simulation to initialize a GeoClaw simulation on real topography, as an illustration of how the tsunami might interact with complex continental shelf geometry. Because the wavelength is quite short relative to the width of the continental shelf, the waves are subject to focusing and de-focusing as they move into shallower water with a smaller wave speed. Figure 15 (left) shows an illustration of the main idea in the context of wind waves focusing on the Northern California shore in a popular surfing area known as Mavericks.

Figure 15 (right) shows the continental shelf bathymetry offshore from the Gray's Harbor region on the Washington Coast. Westport is on the southern peninsula at the entrance to the harbor. The outward curvature of the shelf in this region tends to focus energy towards this region in general, but the wave amplitudes can vary substantially even along this portion of the coast. This is illustrated in Figure 17, which shows the waves approach Gray's Harbor 45 minutes after the airburst.

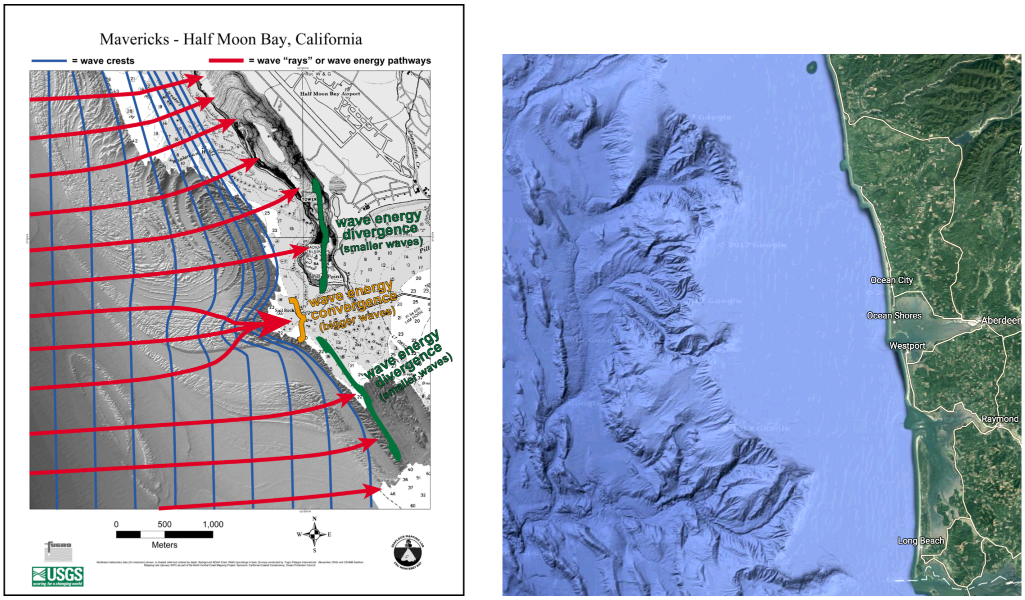

Figure 15. Left: Illustration showing how the geometry of the continental shelf leads to focusing or de-focusing of incoming waves. (Public domain image from the Wikipedia page on Green's Law.) Right: The continental shelf offshore Grays Harbor on the Washington coast, also showing the location of Westport.

Figures 16 and 17 show snapshots from four times taken from the GeoClaw simulation. After 3 minutes, the surface displacement is initialized with a radially symmetric wave form taken from the AG simulation at this time. The fluid velocity is taken to be radially directed outwards, with a speed that is chosen based on the surface elevation in a manner that should give an almost purely outgoing wave on flat topography (based on the eigenvectors of the linearized SWE). The lower plots in Figure 16 show that indeed the waves are primarily outgoing.

The waves propagating toward the deep ocean are not a good approximation of what we would expect to see with a better model such as the Boussinesq equations, since the SWE do not properly model the dispersion of these waves, which have a short wavelength relative to the ocean depth. On the other hand, the waves that immediately propagate onto the continental shelf might be quite accurate since the wavelength is longer here relative to the water depth. We also saw in the parameter study of the previous section that the SWE simulation may at least give an upper bound on the inundation that would be seen with Boussinesq equations.

For this particular location, there is very little inundation anywhere in the Gray's Harbor region for this airburst case, in spite of the generally low lying topography. There is a sandy ridge near the coastline that is about 5 meters elevation and that protects the peninsula.

In Section 4.4 we show a similar simulation for a crater-generated tsunami, in which this region experiences much more extreme flooding.

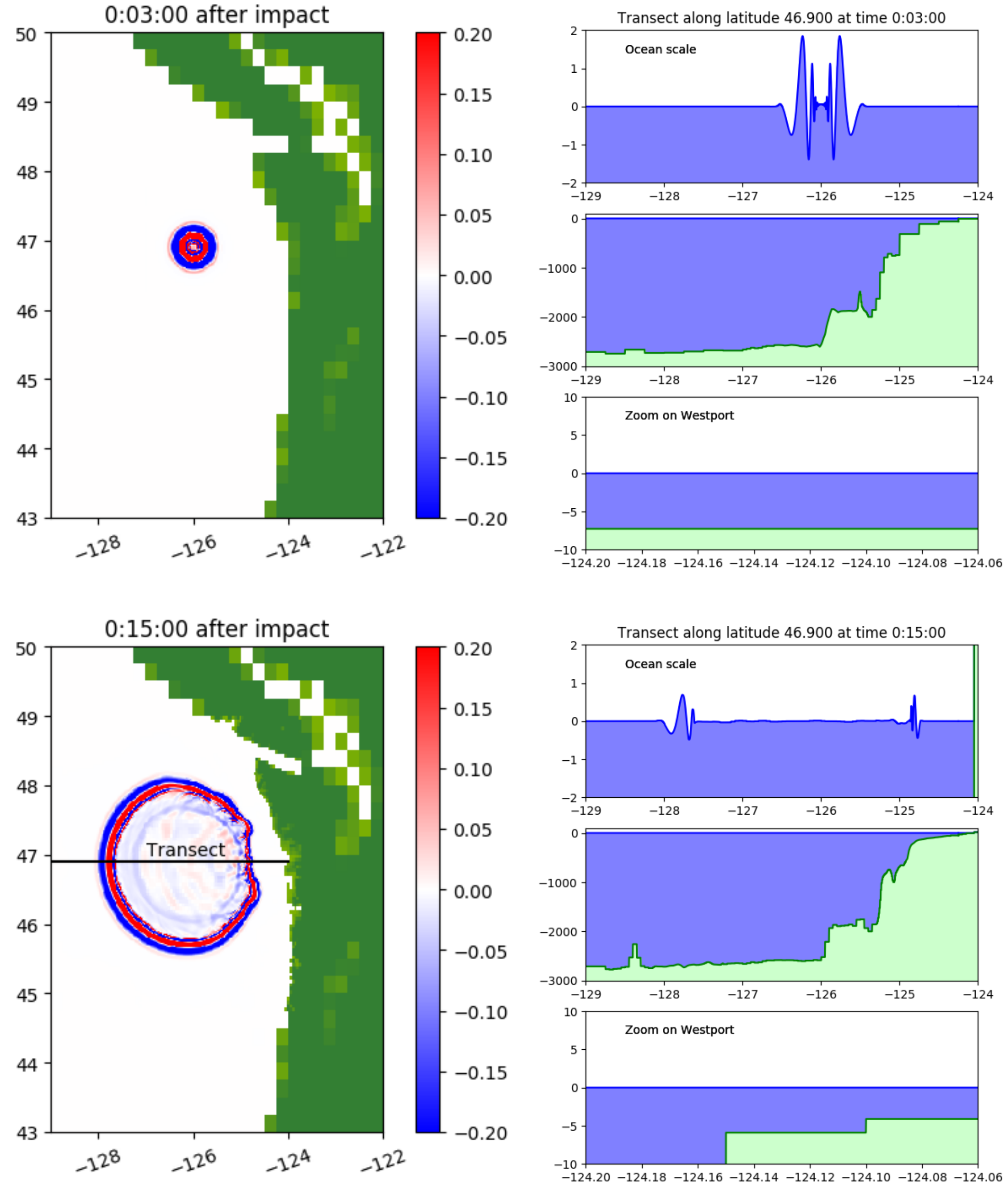

Figure 16. Airburst wave form transferred from the AG code at time 180 seconds (3 minutes), at a location just offshore from the continental shelf. The velocity is set to give an outward expanding shallow water wave. This is propagated forward in time using GeoClaw (SWE), and shown in the bottom plots at time 15 minutes. The plots on the right show cross sections of surface elevation at different scales along the transect shown in the lower left plot. Note that AMR is used and the topography around Westport is not resolved until later times.

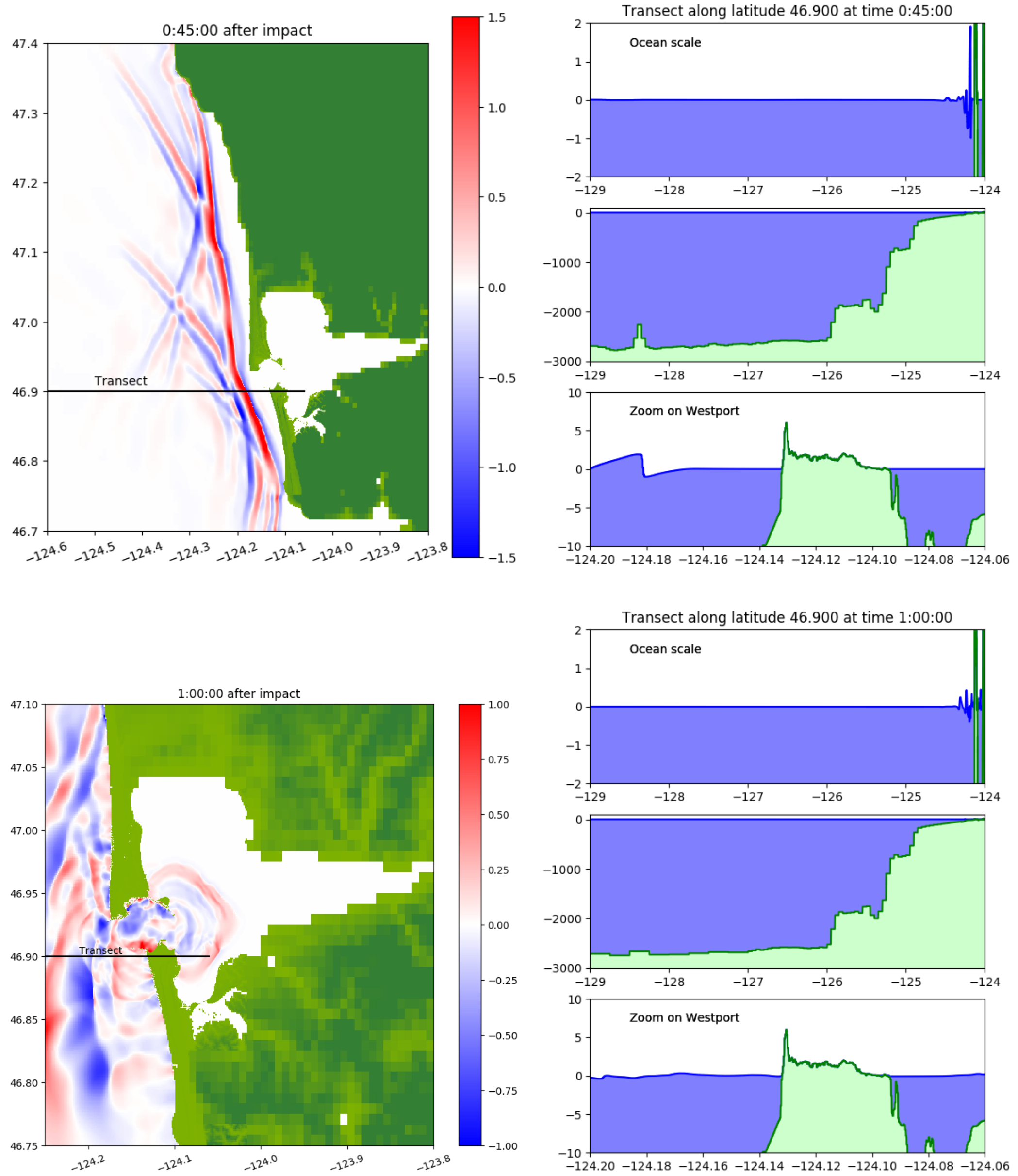

Figure 17. Continuation of simulation from Figure 16 at later times, zoomed around Grays Harbor and Westport, WA.

4 Crater-generated tsunamis

Asteroids above a certain size (depending on the entry angle and other properties) reach the ocean surface and create a crater (in addition to a blast wave that moves over the surface). In extreme cases they can reach the sea floor and create a much more complex crater with solid ejecta, but we have not considered that case. We also ignore the air blast that accompanies the impact since it moves away on a faster time scale.

For this study we have used initial data arising from a *static crater* such as those shown in Figure 2, with an initial deformation of the sea surface and zero velocity, following past studies (e.g. [10]). In Section 4.1 we first explore the tsunami wave that is generated from static crater initial data when various different systems of equations are used. We conclude that it is probably necessary to solve multidimensional equations that include variations in depth in order to generate the correct waves. We compare our results with those obtained by Darrel Robertson using the hydrocode ALE3D [1]. The static crater initial conditions in the SWE or Boussinesq equations gives very different results from ALE3D.

Then, in Section 4.2, we study what happens if we take the results from the ALE3D hydrocode at time $t = 251$ seconds, when it has settled down to a smooth outward moving wave, and transfer the surface elevation and horizontal velocity to initialize a depth-averaged simulation and run that out to later times. We previously found that BoussClaw could accurately propagate the data from airburst data from AG at $t = 180$ seconds out to later times. For the tsunami generated by a crater this is not as successful, as we discuss below in Section 4.1.

Initializing any code with a static crater may give useful bounds along with insight into the behavior of the models, but is not a realistic model of an asteroid impact. In the future it would be desirable to initialize the tsunami using results from a much more complex multidimensional *multiphysics hydrocode* that models the full depth of the ocean during the splashing phase, including for example momentum transfer, temperature changes and vaporization of part of the ocean. However, we believe it is first necessary to better understand the static crater initial data and develop approaches that can efficiently model the resulting tsunami (and its onshore inundation) before moving on to more complex initial data.

After discussing the static crater initialization, in Section 4.3 we present a parameter study analogous to that of Section 3.3, where the shelf length and depth of the deep ocean are varied and the 1D radially symmetric SWE or Boussinesq equations are solved for $t > 251$ using the ALE3D simulation as initial data. Even though the initial crater is not realistic, this parameter study gives some indication of the relation between Boussinesq and SWE results for tsunamis that have large amplitude and short wavelength relative to the ocean depth. As in the case of airburst tsunamis, these results indicate that SWE simulations may at least give an upper bound on the inundation that would be observed if more accurate equations are solved.

Finally, in Section 4.4, we show that we can also use the ALE3D solution to initialize a GeoClaw simulation of the tsunami on real topography. We use the same location as in the example shown in Section 3.4, but now the resulting tsunami inundates all of Westport and Ocean Shores, on the other peninsula bounding Gray's Harbor.

4.1 Initialization with a static crater

To begin the discussion of asteroids that impact the ocean, we compare all models using initial conditions of a static crater. This removes a lot of the complication in the comparisons. In the next sections we will use a full hydrocode simulation of an asteroid impact.

We compare all the models used above (SWE, two Boussinesq codes, and AG) with a hydrocode that starts from a simple crater of known shape (the parabolic crater without lip, as shown in Figure 2) and zero velocity. The crater is one kilometer deep in a 4 kilometer deep ocean. The radius of the crater is 1.5 km. In [10] Ward and Asphaug estimate that a crater of this size comes from an asteroid with radius 40 m, along with their density (3 gm/cc) and entry speed estimates (20 km/sec), with total energy .0115/.155. However there is much debate about this. Robertson's calculations [2] suggest that the tsunami energy used in [10] may be an order of magnitude too large. His results indicate a crater this size could be generated by a 1GT meteor.

Figure 18 shows six snapshots with the above initial conditions. The ALE3D hydrocode results are the from Darrel Robertson as discussed above. The shallow water results are completely wrong, consisting of a single bore traveling with a wave speed over twice the others. We also expect the AG results to be completely wrong, since an initial cavity of this size is out of the linear regime.

Both the Boussinesq results have the same qualitative features in wave amplitudes and wave lengths. The generation is incorrect, but the resulting waves travel at roughly the same speed, lagging each other by approximately 5 seconds. They appear qualitatively similar to the hydrocode results, giving us hope that although the initial generation of waves from the cavity is not well simulated by a depth-averaged model, we might be able to initialize the depth-averaged codes from the ALE3D simulations and propagate them more efficiently. We do this in the next sections. The hydrocode results show large waves in the cavity that continue until approximately 200 seconds, which does not happen in the other simulations. The ALE3D results generate waves of varying amplitudes, and it is evident that the longer wavelengths travel faster.

4.2 Initialization from a hydrocode

In Figure 19 we take the ALE3D hydrocode simulation of the wave produced by a static crater at time $t = 251$ seconds and use this as initial conditions for the Boussinesq equations with parameter $\mathcal{B} = 1/15$. The velocity in the Boussinesq equations is initialized by depth-averaging the velocity computed in the ALE3D code. The left column of this figure shows that at later times the Boussinesq equations do not do as good a job of propagating this wave form to later times as what we observed earlier in Figure 8 for airburst tsunamis. This is because the crater-generated tsunami

---

[2] personal communication

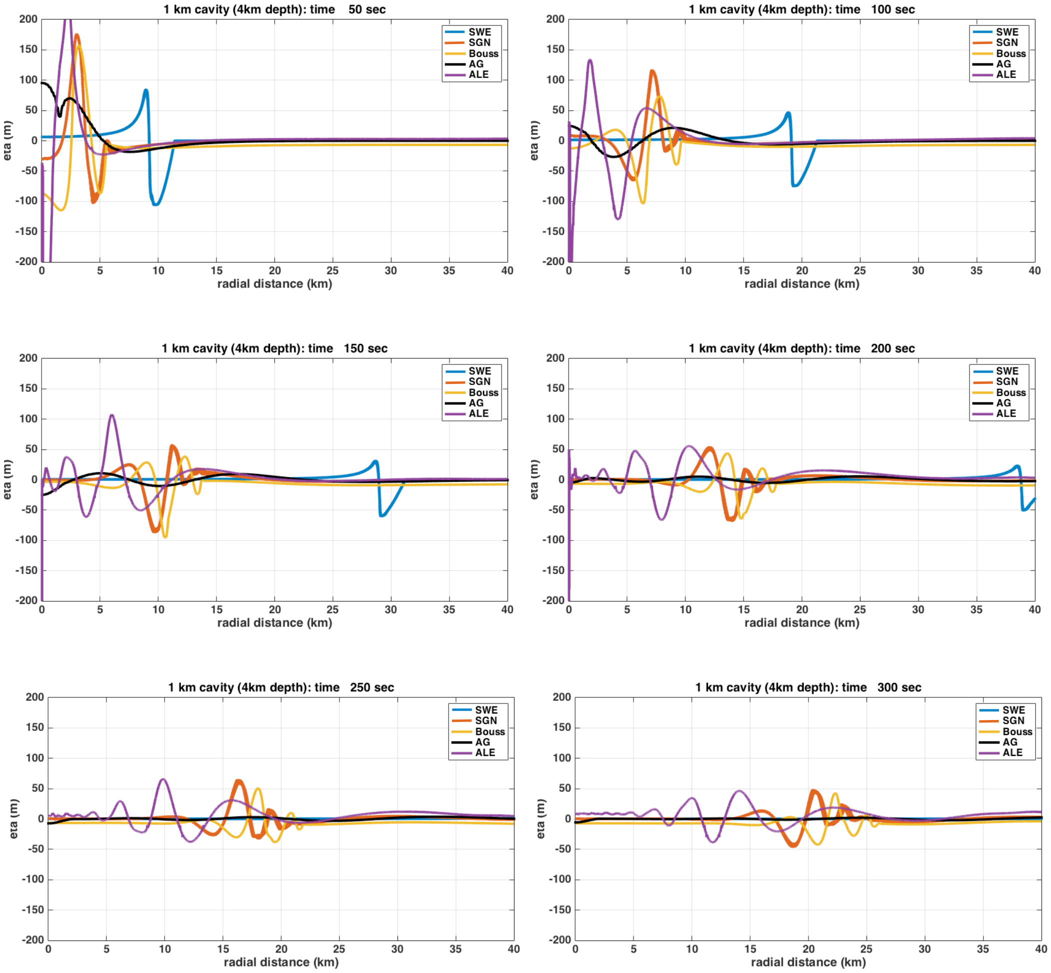

Figure 18. Comparison of all depth-averaged models with ALE3D hydrocode results every 50 seconds, starting from initially static crater.

has a much shorter wavelength, beyond the limit of what can be well modeled by the Boussinesq equation. The largest wave at the final time has a wavelength of around 4 or 5 km, so the parameter on the horizontal axis of the plots shown in Figure A1 is close to 1 since the ocean depth is 4 km. In spite of the limited fidelity, the Boussinesq solution does at least propagate a wave with roughly the correct amplitude and speed.

On the other hand, the right column of Figure 19 shows that transferring the same initial conditions to the shallow water equations gives results at later times that do not agree at all well with later frames from the ALE3D solution. We have tested two different ways of initializing the velocity, either taking the depth-averaged velocity u from the ALE3D data (as was done for Boussinesq), or setting the velocity to be $u = \eta\sqrt{g/h}$ where η is the surface displacement and h the depth. For the shallow water equations this gives a purely right-going wave. Using the ALE3D velocity to initialize SWE gives initial data that splits into left- and right-going waves and gives considerably more energy propagating back toward $r = 0$ (the initial crater location). In both cases the right-going shallow water waves move much faster than the ALE3D or Boussinesq waves.

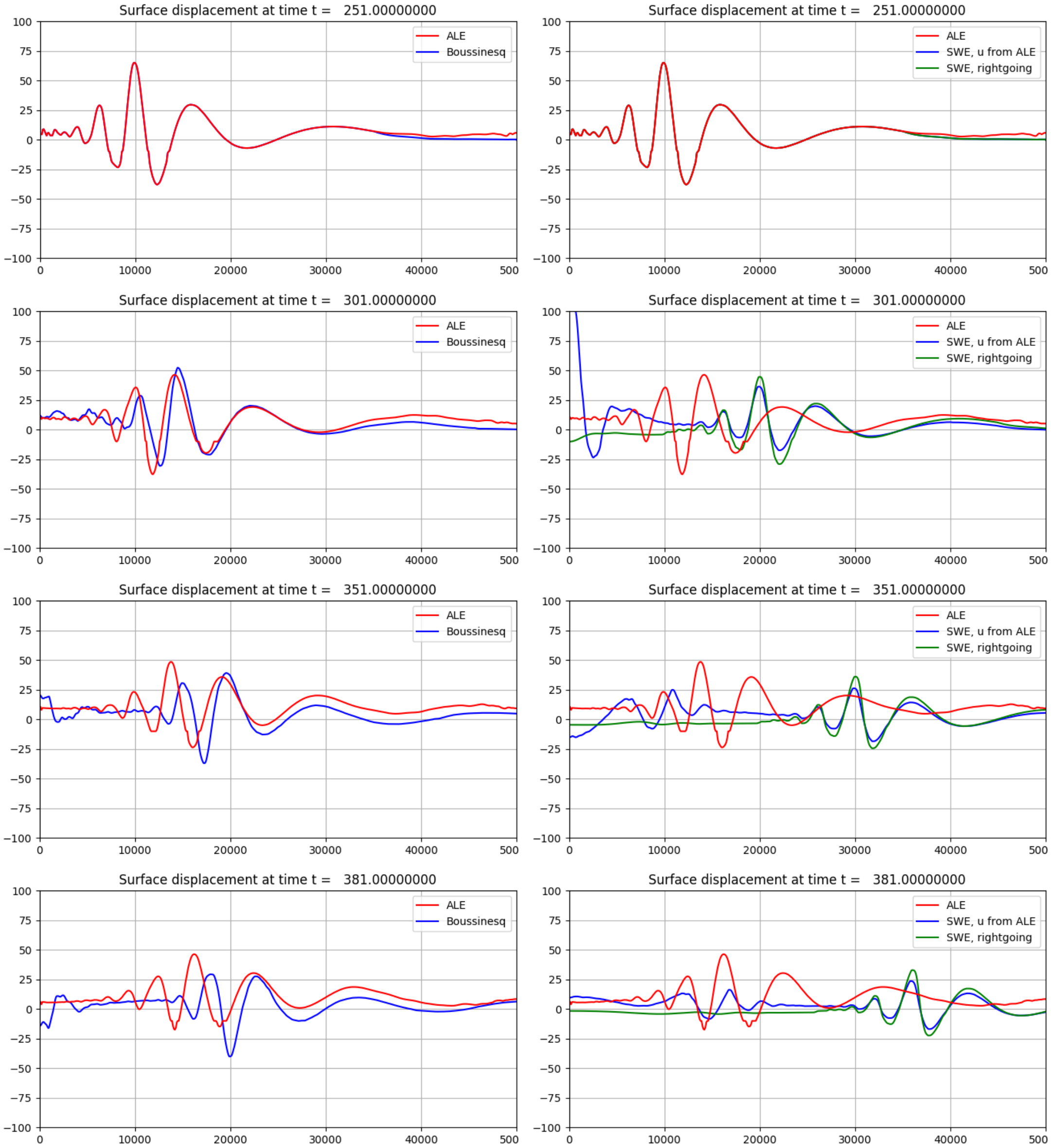

Figure 19. Crater wave form transferred from the hydrocode at time $t = 251$ seconds to the Boussinesq equations using BoussClaw (left column) or to the shallow water equations (right column).

The same difficulties with Boussinesq propagation initialized with static crater hydrocode data were found when we initialized the codes using ALE3D data from a full asteroid water impact simulation. We tried several experiments where we initialized the Boussinesq codes with data extracted at a given time ($t = 15$ seconds, 300 seconds, 796 seconds), and compared with ALE3D results from a later time. As expected, this was no better than the static crater results above, and in fact, this was the motivation for simplifying the problem and looking just at propagation from an initial crater without additional complicating physics.

4.3 Parameter study

Here we repeat the parameter study discussed in Section 3.3 using the crater wave form at $t = 251$ seconds as initial data, and then solving either the 1D radial Boussinesq equations with $\mathcal{B} = 1/15$ or the 1D radial shallow water equations on the same set of piecewise linear topographies, again varying only the length of the deep ocean and continental shelf segments. Comparing Figure 20 to the corresponding plot in Figure 12 for the airburst case, we see that the amplitude of runup is much larger but a similar pattern is observed. The shallow water equations solutions with zero shelf length again provide an upper bound for the runup.

These results should be viewed with caution since there are still many unresolved issues regarding the ability of the Boussinesq equations to properly model these extreme waves.

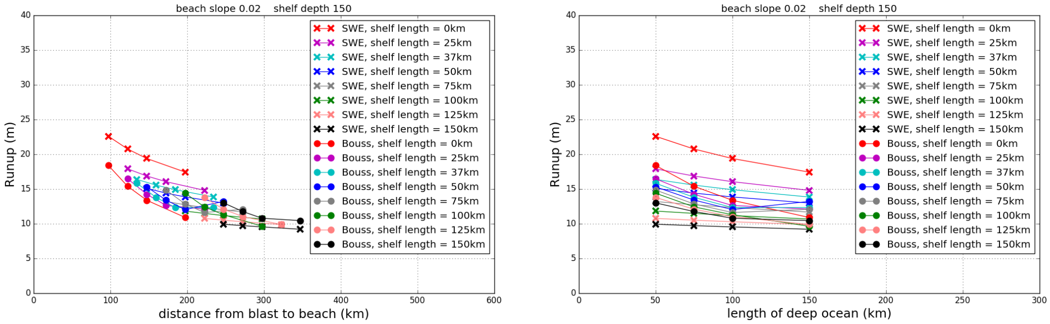

Figure 20. Parameter study comparing SWE and BoussClaw (1D with radial source terms, $\mathcal{B} = 1/15$) in a study of shoreline runup. The solution is initialized from an ALE3D simulation of a 1000 m deep crater at time $t = 251$ seconds, before the waves hit the continental slope. The ocean depth is 4000 m and the shelf depth is 150 m. '×' is a shallow water solution, and '•' is a BoussClaw solution.

4.4 Propagation and inundation on real topography

We initialize a GeoClaw simulation on the same topography as used in Section 3.4, offshore from Gray's Harbor and Westport, WA. We use the radially-symmetric ALE3D simulation results at 251 seconds for the surface displacement. As in the airburst case, we initialize the fluid velocity by assuming an outgoing shallow water wave so as to minimize ingoing waves when the SWE are used to propagate this initial data further in time. Again the wave going toward the deep ocean lacks the dispersion that we would expect in reality, but we are only interested in the wave going onto the shelf and towards shore. Even this wave may be far from correct in the crater case, since the wavelength is smaller than in the airburst case and the amplitude is much larger. Shocks form on the continental shelf when using the SWE that would not form in the Boussinesq equations, where instead the dispersion should lead to generation of more waves of smaller wavelength that remain smoother until approaching shore.

These results are presented primarily to illustrate that GeoClaw can propagate extreme waves and model extensive inundation. Based on our parameter study, we believe they might also give an upper bound on the inundation that would be produced with a more realistic model, but much more work is required to get more quantitative results.

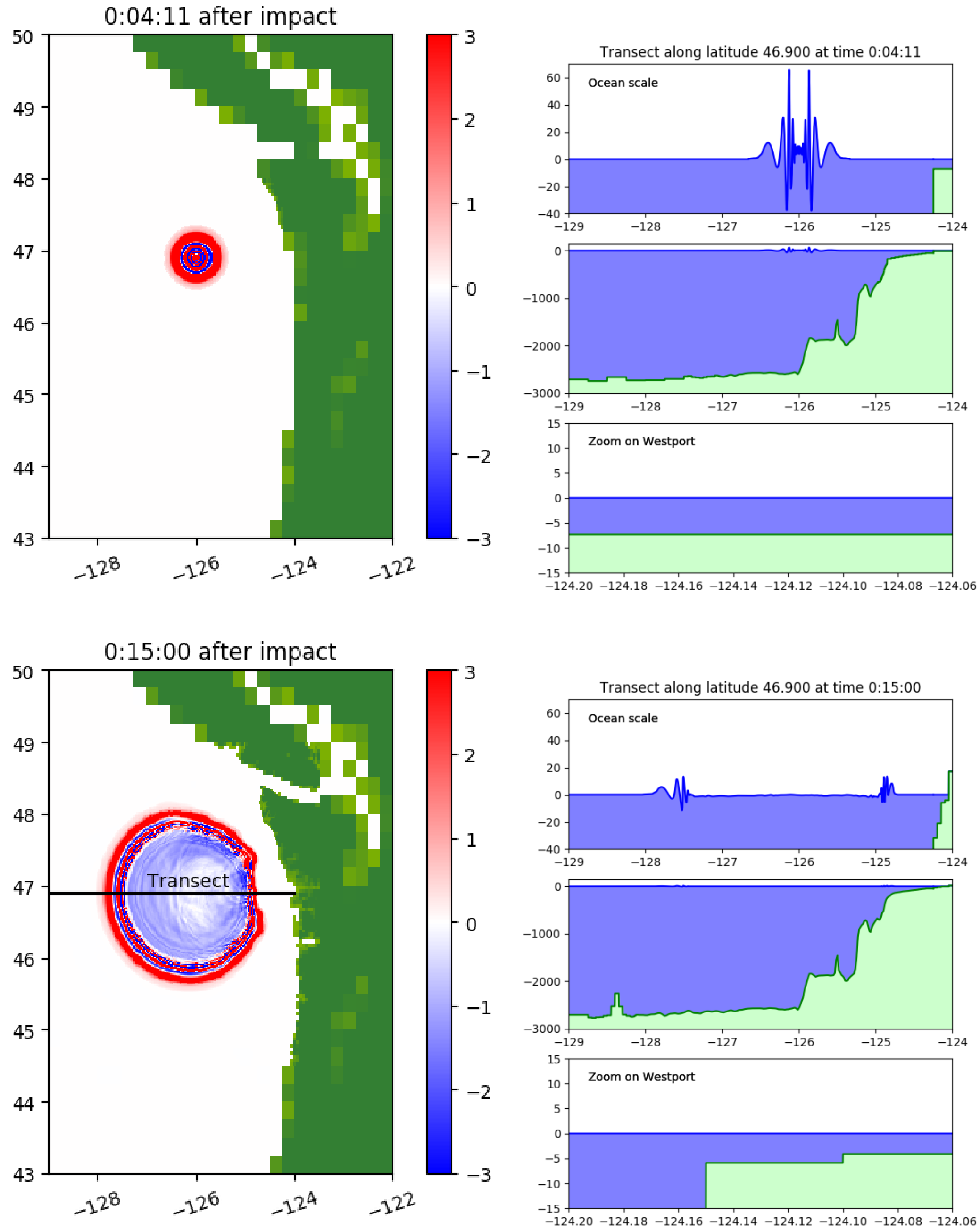

Figure 21. Crater wave form transferred from the AG code at time 120 seconds (2 minutes), at a location just offshore from the continental shelf. The velocity is set to give an outward expanding shallow water wave. This is propagated forward in time using GeoClaw (SWE), and shown in the bottom plots at time 14 minutes. The plots on the right show cross sections of surface elevation at different scales along the transect shown in the lower left plot. Note that AMR is used and the topography around Westport is not resolved until later times.

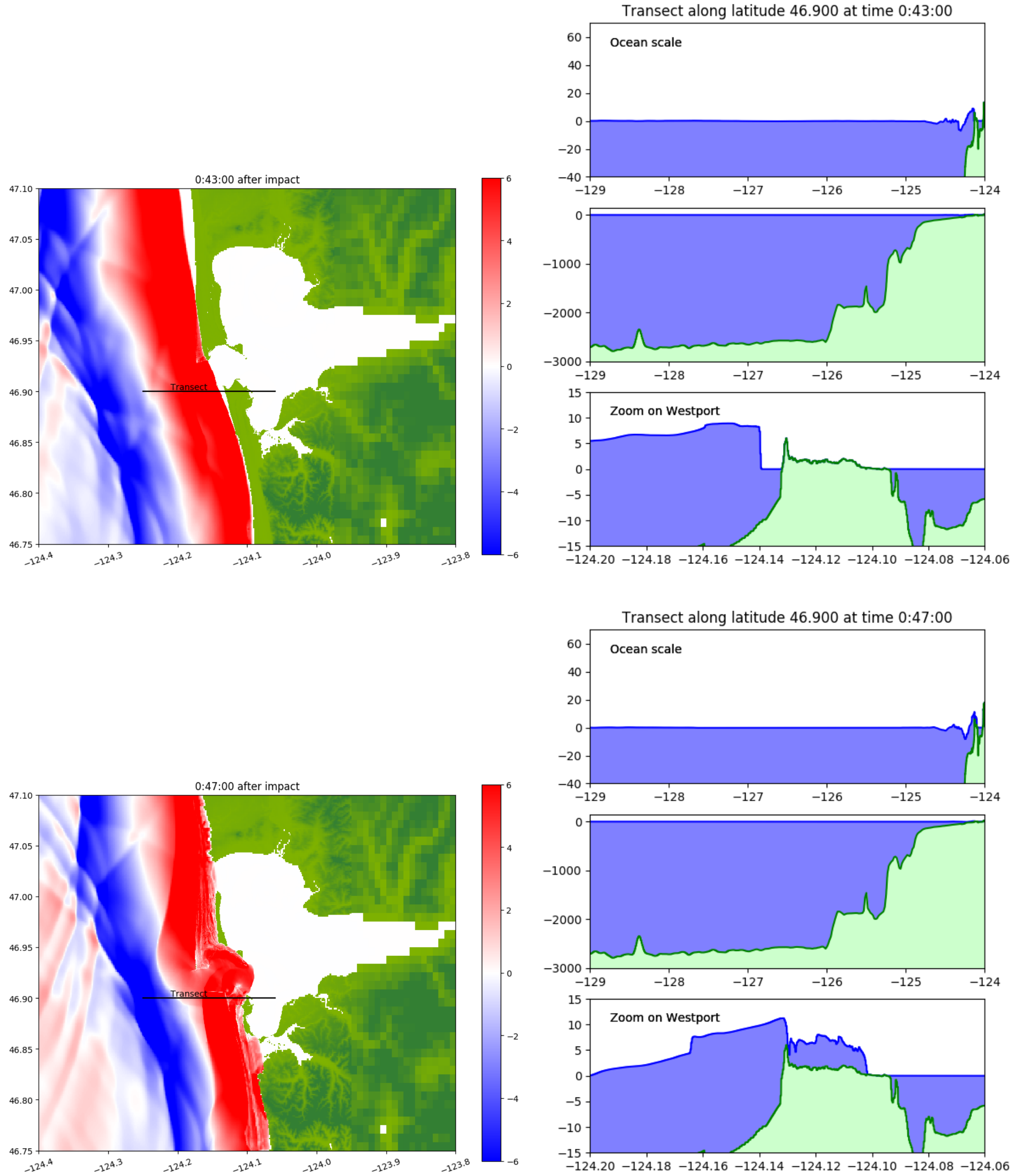

Figure 22. Continuation of simulation from Figure 21 at later times, zoomed around Grays Harbor and Westport, WA.

5 Summary and Conclusions

We summarize our conclusions in this bulleted list, followed by recommendations of directions for future research.

Airburst Summary:

- For airburst asteroids, we have found that the depth-averaged models considered (shallow water equations and Boussinesq) are not able to accurately simulate the initial generation of the main tsunami. Instead we used the linear Euler / acoustics plus gravity (AG) model to generate this wave. We believe that this is a more quantitatively correct representation of the gravity waves generated by airbursts.

- We showed that we can take the wave form generated by AG and transfer it at time $t = 180$ seconds to the Boussinesq equations. Propagating forward in time then matches later results from AG provided we use the BoussClaw model with $\mathcal{B} = 1/15$. Using the SWE model from the same starting data does not match well at later times.

- We showed the previous result still holds as wave shoaling occurs at later times onto a shallow continental shelf.

- A parameter study was performed to vary the shelf length and the length of the deep ocean between the airburst location and the shelf, to see how the runup on a beach varies with these parameters. Simplified geometry and the 1D radially symmetric SWE and BoussClaw were compared, producing Figure 12. The runup decreases with distance of airburst to shore, but results depend on the relative length of the shelf and deep ocean. We also found that the shallow water equations results are generally an upper bound on the (presumably more correct) Boussinesq results, at least for the geometries studied.

- For the radially-symmetric topography and the gently sloping beach used in the parameter study, we found that runup of 3 meters or more might be observed for a 250 MT airburst, even when the airburst distance from shore is more than 100 km. Note from Figure 1 that within a radius of about 60 km of the airburst, 50% fatalities can be expected from the blast wave itself, independent of a tsunami.

- We used the wave form generated by AG at 180 seconds to initialize a GeoClaw simulation with a radially symmetric wave at the edge of the continental slope offshore Westport, WA. We then used GeoClaw (shallow water equations) to propagate that wave onto the shelf and to model inundation. We believe shallow water equations are useful in this case since on the shelf the wavelength is long relative to the water depth, and because our parameter study indicated that SWE results may at least give an upper on what would be observed with Boussinesq equations. We found very little inundation for this particular location, but noted that the wave structure depends very much on the shelf geometry and the runup depends greatly on the beach and onshore topography, so this was presented as an illustration of the sort of site-specific simulations that could be done for airbursts. In view of the parameter study, this one sample simulation does not allow us to conclude that airburst tsunamis will never inundate.

Crater Summary:

- For crater tsunamis, depth-averaged codes cannot model the initial generation of the tsunami since the vertical variation is critical at early times when the crater depth is 1000 m, for example, as used in our study. Moreover the AG code is also not suitable since this code comes from linearizing the Euler equations about a state at rest, assuming the displacement of the surface is very small relative to the ocean depth.
- In our study we used initial data provided by Darrel Robertson that came from running a 2D radially-symmetric version of the hydrocode ALE3D [1] with a static crater initial condition. At time $t = 251$ seconds we transferred the wave form, along with depth-averaged horizontal velocity coming from the hydrocode, to the Boussinesq equations. Running forward in time we got reasonable agreement of the Boussinesq solution with later frames from the hydrocode simulation, in terms of wave amplitude, but the wave length is much shorter than in the airburst case and so Boussinesq was not as good a model. We did show that it is much better than SWE, however.
- We repeated the parameter study (varying shelf and deep ocean length) for the crater initial conditions and found similar results as in the airburst case, in the sense that the shallow water runup generally provides an upper bound on Boussinesq runup, although the magnitudes are much larger in this case than for the airburst case.
- For both airburst and cavity tsunamis, the parameter study revealed an interesting phenomenon that, for a fixed distance from impact to shoreline, with shallow water equations the runup is largest with a short shelf, while for Boussinesq the runup is smallest with the shorter shelf.
- We used the radially symmetric hydrocode data at 251 seconds to initialize GeoClaw off-shore from Westport, WA, similar to what was done in the airburst case. With this hypothetical event, the entire Westport peninsula is overtopped and flooding depths exceed several meters. This illustrates that GeoClaw can be used to model extreme inundation. But this was done using shallow water equations only, and more work needs to be done to determine whether these results are realistic or are overly pessimistic for this size event, as might be suggested by the parameter study.

Recommendations and Future Work:

- We believe that the AG equations can be used to generate radially-symmetric airburst asteroid tsunamis, but this needs further validation. We can then transfer this solution to depth-averaged equations. For airbursts that occur over relatively flat ocean and close to the continental shelf, this may be adequate. Adding bottom bathymetry to a full 3D AG formulation could be explored in the future as a way to propagate an airburst tsunami over the deep ocean, but may not be a high priority since airbursts far from shore cause small tsunami inundation.

- It is possible that better source terms can be derived for the Boussinesq equations that would allow using depth-averaged equations to also generate the airburst tsunami. But it is also possible that depth-dependent effects are significant in the early phases of tsunami generation and that this cannot be done. This is a future research problem.

- For static crater initial conditions, the linearized AG model is inadequate to generate the tsunami and a multidimensional hydrocode must be used to generate the wave form.

- Results from a hydrocode simulation can be transferred to depth-averaged equations at a later time. We showed that Boussinesq equations are not as good at modeling the later phases of the tsunami propagation for these short wavelengths as they were for the airburst tsunami. We had even more trouble trying to transfer hydrocode results coming from a full impact simulation on the Japan Trench to the depth-averaged equations, as would be required for future work with more realistic craters. This requires further study.

- For site-specific hazard studies we believe it is necessary to have a two-dimensional depth-averaged model that can accurately propagate a tsunami onto the continental shelf and onshore, since full three-dimensional modeling is not practical for inundation studies. The GeoClaw model using the shallow water equations may be adequate for airburst tsunamis and might at least give an upper bound for larger-amplitude shorter-wavelength tsunamis arising from cratering asteroids. The parameter study of Figure 20 suggests this, but also shows the SWE results being much larger, which for these large-amplitude events would make a significant difference in how far inland the tsunami propagates as well the depth of flooding.

- Ideally, a two-dimensional Boussinesq code that handles general topography and also inundation modeling would be useful, particularly for crater cases. We explored use of the Basilisk software, but found it too rigid for our purposes, and although it works in parallel, it is not easily adaptive. For future work, adaptive mesh refinement in a Boussinesq code is critical since it is necessary to model coastal regions at much higher resolution than offshore to perform hazard assessments.

- The BoussClaw code is also not yet adaptive. Solving the Boussinesq equations requires solving an elliptic equation in each time step and/or using an implicit method for time stepping. Implementing this in the context of AMR in BoussClaw is a major undertaking. The 2D BoussClaw software without AMR could be used for some purposes, but has not yet been carefully tested. Based on our experience in 1D, we believe it requires some improvements, but this should be relatively easy to do compared to adding AMR.

Appendix A

Details of model equations and numerical implementations

A.1 Shallow water equations

The shallow water equations (SWE) are depth-averaged equations modeling the depth $h(x, y, t)$ and the depth-averaged velocities $u(x, y, t)$ and $v(x, y, t)$ in two horizontal directions. Letting $\vec{u} = (u, v)$, the equations can be written as

$$\begin{aligned} h_t + \nabla \cdot (h\vec{u}) &= 0, \\ (h\vec{u})_t + u\nabla \cdot (h\vec{u}) + (h\vec{u} \cdot \nabla)\vec{u} + \frac{1}{2} g \nabla (h^2) &= -gh\nabla B, \end{aligned} \tag{A1}$$

where $B(x, y)$ is the sea floor bathymetry (where $B < 0$) or onshore topography (where $B > 0$). The first equation gives conservation of mass. If $B \equiv$ constant (a uniform flat sea floor) then the right hand side reduces to 0 and the second equation gives conservation of momentum.

In one space dimension these equations reduce to

$$\begin{aligned} h_t + (hu)_x &= 0, \\ (hu)_t + \left(hu^2 + \frac{1}{2} g h^2\right)_x &= -ghB_x. \end{aligned} \tag{A2}$$

These equations model plane waves in which there is no $v \equiv 0$ and there is no variation in the topography, initial conditions, or solution in the y direction.

For asteroid impacts a more relevant special case is radially-symmetric solutions where the initial conditions and solution are assumed to vary only with distance r from the center and the azimuthal velocity is assumed to be zero. Of course for solutions to have this form the topography $B(r)$ must also vary only with r. The 2D equations can be written in polar coordinates and then assuming no variation in the θ direction and letting $U(r, t)$ denote the radial velocity, the equations reduce to

$$\begin{aligned} h_t + (hU)_r &= -\frac{1}{r}(hU), \\ (hU)_t + \left(hU^2 + \frac{1}{2} g h^2\right)_r &= -(hU^2)/r. \end{aligned} \tag{A3}$$

Bottom friction drag terms are usually also added to the momentum equations in any of these formulations, which become important in very shallow water near the coast and for properly modeling inundation and onshore propagation. We use a standard Manning friction term with coefficient $n = 0.025$, as recommended for generic tsunami inundation modeling.

Details about how these equations are solved numerically in the GeoClaw software can be found in the papers [14, 15].

A.2 Dispersion

The shallow water equations are derived from three-dimensional fluid equations by making two assumptions: that the wavelength of the wave modeled is long relative to the fluid depth and that the amplitude is small relative to the depth. However, they have been shown to work well for modeling nonlinearities in very shallow depths near shore, including bore formation (which appears as discontinuous shock waves in the shallow water equations), and for modeling inundation providing the wetting-and-drying is handled well. They break down, however, for waves with short wavelength relative to the fluid depth as these waves propagate over long distances. In this case the 3D equations exhibit dispersive behavior, where the propagation velocity depends on the wavelength, and hence an initial Gaussian-shaped wave, for example, will spread out into an oscillatory wave train with each wave number propagating at its own group velocity, which can be calculated from the dispersion relation of the model equations. If we consider a monochromatic translating wave of the form

$$\eta(x,t) = \eta_0 \exp(i(\xi x - \omega t)), \tag{A4}$$

and a similar expression of the velocity, then plugging this into the equations gives the *dispersion relation* relating ω to ξ. The group velocity for wave number ξ is given by the derivative of this relation, $d\omega(\xi)/d\xi$.

If the fluid dynamics equations in a vertical cross section of the ocean are linearized then the dispersion relation can be worked out for the “Airy solution” to these equations. Rather than plotting the dispersion relation, we plot the group velocity which is more meaningful and convenient to look at in relation to the speed at which waves are expected to propagate. The group velocity for the Airy solution is shown in Figure A1 as a function of the wave length normalized by the fluid depth, and where the vertical axis shows the group velocity divided by $\sqrt{gh}$. The linearized shallow water equations are non-dispersive, and all waves propagate at the same speed $\sqrt{gh}$, also illustrated in Figure A1. Note that for the Airy solution, the group velocity approaches the shallow water speed for long wave lengths, but decreases and approaches 0 for short wave lengths. The other two curves correspond to two versions of Boussinesq equations described below with parameter choices $\mathcal{B} = 0$ (the Peregrine equations) and $\mathcal{B} = 1/15$, as we typically use in the BoussClaw code.

A.3 Shoaling

As a wave train moves from deep water into shallower water and the wave speed decreases, the spatial wavelength of the wave also decreases, while the amplitude of the wave typically increases. Consider small amplitude waves on an ocean depth that changes from h_ℓ in the ocean to h_r on the shelf, for example, and let A_ℓ and A_r be the corresponding amplitudes.

For linearized shallow water with a continental slope that rises slowly relative to the wavelength, there is very little reflected energy at the slope and the amplitude increase follows *Green’s Law*,

$$A_r/A_\ell = (h_\ell/h_r)^{1/4}. \tag{A5}$$

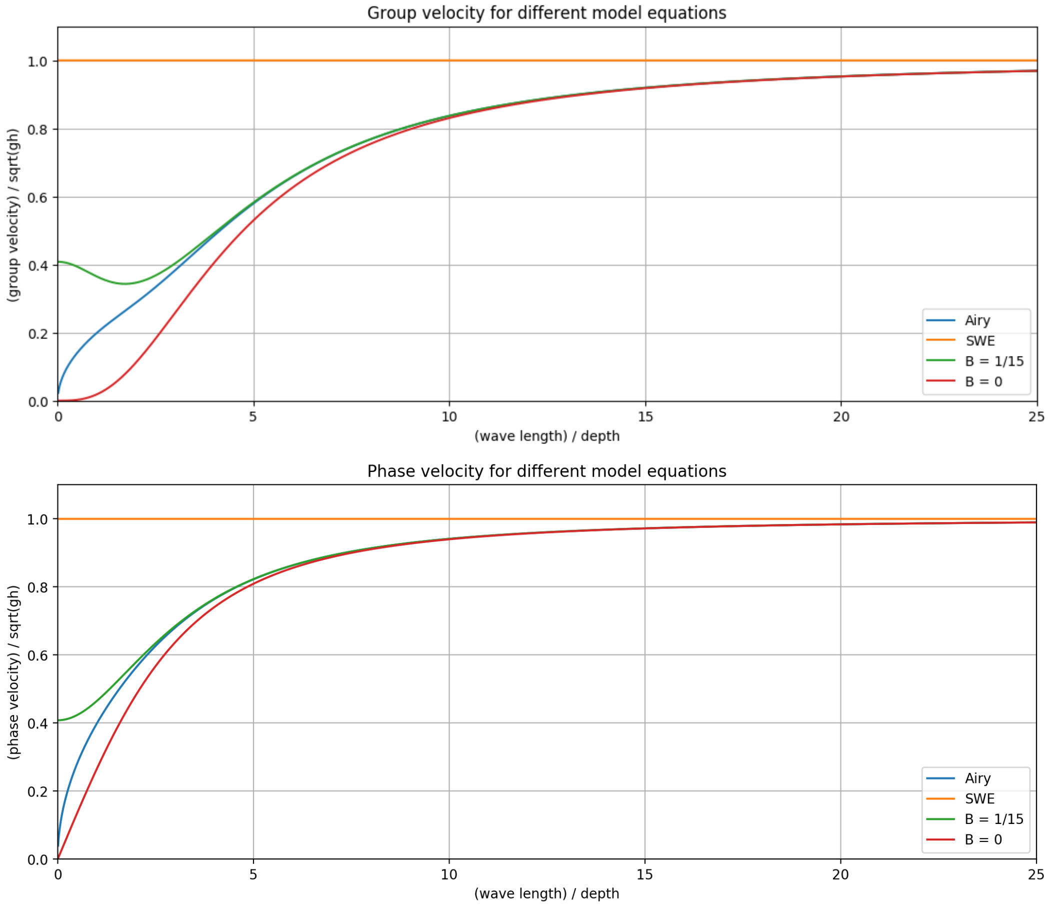

Figure A1. Plots of the ratio of group velocity to the shallow water wave speed $\sqrt{gh}$ as a function of the ratio of wavelength to fluid depth, and a similar plot of the phase velocities.

This can be found via conservation of energy in a Gaussian pulse, for example, by assuming the wave has the form $A_\ell \eta_0((x - c_\ell t)/c_\ell)$ before hitting the shelf and $A_r \eta_0((x - c_r t)/c_r)$ on the shelf, with $c_{\ell,r} = \sqrt{h_{\ell,r}}$. Equipartition of energy holds on each side and so we can consider the potential energy alone, for example, which is $g \int_{-\infty}^{\infty} \eta(x,t)\,dx = gA^2c^2 \int_{-\infty}^{\infty} \eta_0(y)\,dy$ and equating this for the two sides gives (A5).

Alternatively, one can look at a monochromatic Fourier mode $\exp(i(\xi x - ct))$ with amplitude $A(x)$ and work out that $A'(x)/A(x) = -0.25h'(x)/h(x)$ provided ξh_ℓ is sufficiently small that the shallow water equations are valid. Integrating this between a point in the deep ocean and a point on the shelf gives $\log(A_r) - \log(A_\ell) = 0.25(\log(h_\ell) - \log(h_r))$, and exponentiating again gives (A5).

For Boussinesq equations the wave velocity is slower than $\sqrt{gh}$ for short wavelengths and so the shoaling equation changes. In general it is possible to derive an expression of the form $A'(x)/A(x) = -\alpha_5 h'(x)/h(x)$ where we follow the notation of [3] and call the parameter α_5 the *shoaling gradient*. This parameter varies with ξh and replaces 0.25 in Green's Law (A5) when studying waves that are short relative to the fluid depth.

According to [3], the linearized Airy wave solution has

$$\alpha_5 = \frac{G\left(1+\frac{1}{2}G(1-\cosh(2\xi h)\right)}{(1+G)^2} \tag{A6}$$

where $G = 2\xi h/\sin(2\xi h)$. Taylor expansion of (A6) gives $\alpha_5 = \frac{1}{4}\left(1-(\xi h)^2+\cdots\right)$ as $\xi h \to 0$, showing the connection to Green's Law for wavelengths $L = 2\pi/\xi$ that are long compared to h. The shoaling gradient can also be calculated for Boussinesq equations and compared with the expression (A6), see Section A.4.2.

A.4 Boussinesq equations

There are several forms of "Boussinesq equations" that have been introduced and studied over the past several decades.

A.4.1 Peregrine equations

One of the earliest proposals for depth-averaged equations to better model dispersion was Peregrine's model, see [4]. In 2 dimensions on a variable bottom, let $\vec{x} = (x, y)$ and as before $\vec{u} = (u, v)$ and let $h_0(\vec{x})$ be the undisturbed depth. Then the equations take the form:

$$\begin{aligned}
&h_t + \nabla\cdot(h\vec{u}) = 0 \\
&(h\vec{u})_t + gh\nabla\eta + (h\vec{u}\cdot\nabla)\vec{u} + \vec{u}\,\nabla\cdot(h\vec{u}) \\
&\qquad + \frac{1}{6}h_0^3\nabla(\nabla\cdot((h\vec{u})_t/h_0) - \frac{1}{2}h_0^2\nabla(\nabla\cdot(h\vec{u})_t) = 0.
\end{aligned} \tag{A7}$$

If the higher-derivative terms on the last line are dropped, these reduce to the 2D SWE. If the bottom if flat ($h_0 \equiv$ constant) then the higher-derivative terms reduce to $\frac{1}{3}h_0^2\nabla(\nabla\cdot(h\vec{u})_t)$.

In one space dimension, the equations (A7) reduce to:

$$\begin{aligned}
&h_t + (hu)_x = 0 \\
&(hu)_t + gh\eta_x + (hu^2)_x + \frac{1}{6}h_0^3(hu/h_0)_{txx} - \frac{1}{2}h_0^2(hu)_{txx} = 0.
\end{aligned} \tag{A8}$$

Again the last two terms can be combined if h_0 is constant. Also note that $gh\eta_x = \left(\frac{1}{2}gh^2\right)_x - g\eta(h_0)_x$, the form typically used in the conservative form of the SWE, with $g\eta(h_0)_x$ moved to the right hand side as the topographic source term.

To derive the 1D equations with radial source terms, we can assume that

$$\vec{u}(x, y, t) = (U(r, t)\cos(\theta), U(r, t)\sin(\theta))$$

in polar coordinates, where $U(r, t)$ is the radial velocity, and then assume the topography h_0 varies only with r and that the initial data and solution are functions of r, t only, constant in the θ direction. The r-component of the gradient ∇s of a scalar quantity in polar coordinates is just s_r, the divergence transforms to $\nabla\cdot\vec{u} = \frac{1}{r}(rU)_r$, and so $\nabla(\nabla\cdot\vec{u}) = \left(\frac{1}{r}(rU)_r\right)_r$. The Peregrine equations (A7) thus transform to:

$$\begin{aligned}
&h_t + \frac{1}{r}(rhU)_r = 0\\
&(hU)_t + gh\eta_r + \frac{1}{r}(rhu^2)_r + \frac{1}{6}h_0^3\left(\frac{1}{r}(rhu/h_0)_{tr}\right)_r - \frac{1}{2}h_0^2\left(\frac{1}{r}(rhu)_{tr}\right)_r = 0.
\end{aligned} \tag{A9}$$

Alternatively, these can be written as

$$\begin{aligned}
&h_t + (hU)_r = -hU/r\\
&(hU)_t + \left(hU^2 + \frac{1}{2}gh^2\right)_r + \frac{1}{6}h_0^3\left(\frac{1}{r}(rhu/h_0)_{tr}\right)_r\\
&\qquad\qquad - \frac{1}{2}h_0^2\left(\frac{1}{r}(rhu)_{tr}\right)_r = -(hU^2)/r + gh(h_0)_r.
\end{aligned} \tag{A10}$$

Dropping the dispersive terms from this equation gives the conservative form of the 1D SWE with radial and topographic source terms. The dispersive terms are also modified from the pure 1D version of (A8) and give additional radial source terms.

A.4.2 BoussClaw

The Peregrine equations are generally too dispersive and so improved versions have been developed that better match the dispersion relation of the Airy solution to the linearized Euler equations.

The BoussClaw code described in [5] solves the equations discussed by Schäffer and Madsen [7] and Madsen and Sorensen [3]. These equations can be derived by choosing a scalar $\mathcal{B}$, applying the operator $-\mathcal{B}h_0^2\nabla(\nabla\cdot)$ to the terms $(h\vec{u})_t + gh\nabla\eta$ appearing in the momentum equation and then adding this quantity,

$$-\mathcal{B}h_0^2\left[\nabla(\nabla\cdot(h\vec{u})_t) + g\nabla(\nabla\cdot(h\nabla\eta))\right] \tag{A11}$$

to the momentum equation of the Peregrine equations (A7). If $\mathcal{B} = 0$ then of course this just reduces to the Peregrine equations, but it turns out that choosing $\mathcal{B} = 1/15$ gives much better agreement with the dispersion relation. (Don't confuse $\mathcal{B}$ with $B(\vec{x}) = -h_0(\vec{x})$, which is used elsewhere for the bathymetry.) This is illustrated in Figure A1, where the group velocity is plotted for both $\mathcal{B} = 0$ (Peregrine) and $\mathcal{B} = 1/15$. BoussClaw allows setting $\mathcal{B}$ to any value, so it has also been used to compute solutions to the Peregrine equation for various test problems, and we have confirmed that these solutions are generally too dispersive and that $\mathcal{B} = 1/15$ works much better.

Plots in [3] also show that this form of Boussinesq equations with $\mathcal{B} = 1/15$ match the expression (A6) for the shoaling gradient very well, and much better than with $\mathcal{B} = 0$. This suggests that these equations are also very good at modeling the shoaling of waves onto the continental shelf, as was seen numerically in Figure 8.

A.4.3 SGN

The Serre-Green-Naghdi equations start with shallow water equations (A1) and add to the source terms in momentum equations. The right hand side becomes

$$S = -gh\nabla B + h(\frac{g}{\alpha}\nabla\eta - D). \tag{A12}$$

The vector D with components (D_x, D_y) satisfies the complicated second order equation

$$\begin{aligned} &-\alpha h^2\left[\frac{h}{3}\nabla(\nabla\cdot D) + (\nabla\cdot D)\left(\nabla h + \frac{1}{2}\nabla B\right)\right] \\ &\qquad + \alpha h\left[\frac{h}{2}\nabla(\nabla B\cdot D) + (\nabla B\cdot D)\nabla\eta\right] + hD = \frac{g}{\alpha}\nabla\eta + Q_1(u). \end{aligned} \tag{A13}$$

The operator Q_1 is a nonlinear function of h, B, the velocities and their first derivatives. The parameter α in the SGN code used for these experiments is 1.15. For details on SGN and the methods used to solve it see [8] and references therein.

A.5 Acoustics+Gravity equations

In one horizontal dimension x plus depth z, the linearized Euler (AG) equations can be written

$$\begin{aligned} \rho_t + \rho_w u_x + \rho_w w_z &= 0 \\ \rho_w u_t + c_a^2\rho_x &= 0 \\ \rho_w w_t + c_a^2\rho_z &= -\rho g\ . \end{aligned} \tag{A14}$$

In (A14), u is the horizontal velocity, w is the vertical velocity, $c_a = \sqrt{\frac{dp}{d\rho}(\rho_w)} =$ 1500 m/sec is the acoustic speed of sound in water, $\rho_w = 1025\,\mathrm{km/m^3}$ is taken to be constant in ocean water, and g is gravity. These are derived by linearizing the compressible Euler equations around the rest state $u = w = 0$ and ρ is the perturbation in density from ρ_w. Note that the sea level η, or equivalently the height of the water $h = \eta - B$, has not yet appeared.

The three boundary conditions come from linearizing the dynamic, kinematic and pressure boundary conditions for the Euler equations. The boundary conditions become

$$\begin{aligned} &w = \frac{\partial\eta}{\partial t}(x,t) && \text{top} \\ &w = u\cdot B_x && \text{bottom} \\ &c_a^2\rho(x,h_0,t) - \rho_w g\eta = p_{atm}(x,t) && \text{continuity of pressure} \end{aligned} \tag{A15}$$

The right-hand side in the last equation is where the atmospheric overpressure p_{atm} from the Friedlander profile of an airburst appears. For the flat bottom experiments in this report $B_x = 0$, so the bottom boundary condition simplifies to $w = 0$. The boundary condition that gives η can be integrated at every time step to give η (or h) at every x location. We do this by linearly extrapolating w to the top of the domain, and then updating η from the previous time step, $\eta^{n+1} = \eta^n + dt \cdot w(h_0)$, where we use $z = 0$ as the bottom of the domain, and η_0 is the top.

These equations can also be rewritten to use pressure instead of density, using $p = c_a^2 \rho$. If this is done, we implement the boundary conditions in a slightly different way. The boundary conditions are given by setting the pressure at the top boundary to the sum of the atmospheric overpressure p_{atm} and a displacement pressure $\rho_w g \eta$, where η is determined by integrating in time the vertical component of velocity.

Radial source terms were included in the AG model so that this vertical cross section actually models acoustics in a 3D ocean, for the case we consider of radially symmetric bathymetry, initial data, and atmospheric pressure forcing. These terms modify only the first equation in (A14), replacing 0 on the right hand side by $-\rho_w u/r$.

Appendix B

Computer time required

We have not attempted to do a careful comparison of the run times of the various codes used, but report some estimates to give an idea of the relative computational costs.

B.1 Acoustics+Gravity (AG)

The results presented in Section 3.2 and Section 3.2.2 were computed using Clawpack with AMR and OpenMP on a quadcore MacBook Pro. The run up to $t = 100$ seconds shown in Figures 4 and 5 took about 24 minutes of CPU time and 6 minutes of wall time to complete, for the resolution used. A 200×20 grid was used at level 1, with refinement by factors of 4,4 in x and t and $4, 1$ in y at levels 2 and 3 (less in y since there is less variation in the vertical direction). For this two-dimensional calculation, increasing the resolution by a factor of 2 in each direction would increase the computational time by a factor of 8.

The computation of Section 3.2.2 took much longer since it is on a larger domain (100 km by 4 km depth) and goes out to a later time, $t = 1000$ seconds, and we refined with factors 4,2 in y starting from a 500×20 grid. Moreover, the grid mapping used to conform to the shelf results in the grid cells being more compressed in y on the shelf than in the ocean, hence requiring a smaller time step because of the CFL condition. This computation took about 101 hours of CPU time and 35 hours of wall time, again on the same MacBook.

B.2 One-dimensional (radial) shallow water and Boussinesq

The 1D code was run on a nonuniform grid chosen so that the Courant number is close to 1 everywhere in the deep ocean and on the shelf, with the cell size decreasing to a minimum width of 10m near the beach and onshore. Adaptive refinement was not used, since solving the Boussinesq equations requires using an implicit method, which is not yet implemented with AMR.

The run time required depends on the size of the domain and the length of time simulated. As an example, we timed the code for one intermediate case from the case study presented in Section 3.3. We set the shelf length to 50 km and the deep ocean length to 100 km. The entire domain is then approximately 200 km long (including also the continental slope and beach) and 9680 grid cells are used. We estimated that the time for the first wave to reach the beach was approximately 2500 seconds and so ran the calculation out to 4300 seconds (longer than necessary, but we wanted to insure that we captured the largest run-up for the parameter study).

For the Boussinesq code, this case took roughly 7.5 minutes of CPU time on a MacBook. The shallow water version slightly faster, about 5.25 minutes of CPU time on the same computer, since it uses an explicit method. But note that in the 1D case the implicit solver only needs to solve a tridiagonal system of equations which is the same order of magnitude work asymptotically as an explicit method. By contrast, in 2D the Boussinesq code would be much slower than solving the shallow water equations.

B.3 GeoClaw simulations of propagation and inundation

The two-dimensional GeoClaw (SWE) simulation from Section 3.4 was run on a MacBook Pro using AMR and OpenMP with 4 threads, and required about 4 hours of CPU time and 1 hour of wall clock time.

The simulation from Section 4.4 was run on the same MacBook using AMR and OpenMP but with 3 threads, and required about 20 hours of CPU time and 7 hours of wall clock time.

Both simulations were run out to 1 hour of simulated time. The large increase in CPU time required for the crater case is partly because a larger region along the shore was flagged for refinement, but mostly (we think) because there was significant inundation and so more Riemann solutions on this level required the relatively expensive logic of the nonlinear wetting-drying region. By contrast, with the airburst case most of the onshore cells stayed dry, in which case the Riemann solution is trivial and much less work is done to advance these cells. This requires further study.

B.4 SGN simulations

The radially symmetric SGN simulations used the fully two-dimensional Basilisk code on a quarter plane. For one example of timing, the airburst calculation in Figure 6 on a 1024 by 1024 grid took 4 minutes 22 seconds of wallclock time to simulate the first 100 seconds, using 10 cores of an Intel Linux box with Haswell cores. By contrast, the same mesh using the SGN solver in Basilisk took 7 hours 30 minutes of wallclock time. We have no explanation for why this is so much more expensive than the estimate given by Popinet [8] that SGN should be 4-10 times the cost of SWE, and are conferring with him about this.

References

1. Nichols, A. L.; and (Eds.), D. M. D.: ALE3D Users Manual: An Arbitrary Lagrange/Eulerian 2D and 3D Code System. Lawrence Livermore National Laboratory LLNL-SM-726137, 2017.
2. K.T.Mandli; Ahmadia, A.; Berger, M.; Calhoun, D.; George, D.; Hadjimichael, Y.; Ketcheson, D.; Lemoine, G.; and LeVeque, R.: Clawpack: building an open source ecosystem for solving hyperbolic pdes. *PeerJ Computer Science 2:e68*, 2016. Https://doi.org/10.7717/peerj-cs.68.
3. Madsen, P. A.; and Sørensen, O. R.: A New Form of the Boussinesq Equations with Improved Linear Dispersion Characteristics. Part 2. A Slowly-Varying Bathymetry. *Coastal engineering*, vol. 18, no. 3-4, 1992, pp. 183–204. URL `http://www.sciencedirect.com/science/article/pii/037838399290019Q`.
4. Peregrine, D. H.: Long Waves on a Beach. *Journal of Fluid Mechanics*, vol. 27, no. 4, 1967, pp. 815–827. URL `https://www.cambridge.org/core/journals/journal-of-fluid-mechanics/article/long-waves-on-a-beach/7C32E1E0CE1C168D57054F1F1ED43977`.
5. Kim, J.; Pedersen, G. K.; Løvholt, F.; and LeVeque, R. J.: A Boussinesq type extension of the GeoClaw model - a study of wave breaking phenomena applying dispersive long wave models. *Coastal Engineering*, vol. 122, 2017, pp. 75 – 86. URL `http://www.sciencedirect.com/science/article/pii/S0378383917300546`.
6. Madsen, P. A.; and Schäffer, H. A.: Higher–order Boussinesq–type equations for surface gravity waves: derivation and analysis. *Phil. Trans. Royal Soc. A*, vol. 356, no. 1749, 1998, pp. 3123–3181.
7. Schäffer, H. A.; and Madsen, P. A.: Further Enhancements of Boussinesq-Type Equations. *Coastal Engineering*, vol. 26, no. 1-2, 1995, pp. 1–14. URL `http://www.sciencedirect.com/science/article/pii/0378383995000172`.
8. Popinet, S.: A quadtree-adaptive multigrid solver for the Serre-Green-Naghdi equations. *J. Comp. Phys.*, vol. 302, 2015, pp. 336–358.
9. Kranzer, H.; and Keller, J.: Water Waves Produced by Explosions. *J. Applied Physics*, vol. 30, no. 3, 1959, pp. 398–407.
10. Ward, S. N.; and Asphaug, E.: Asteroid Impact Tsunami: A Probabilistic Hazard Assessment. *Icarus*, vol. 145, 2000, pp. 64–78.
11. Aftosmis, M.; Mathias, D.; Nemec, M.; and Berger, M.: Numerical simulation of bolide entry with ground footprint prediction. *AIAA-2016-0998*, 2016.
12. Berger, M. J.; and Goodman, J.: Airburst Generated Tsunamis. *Pure Appl. Geophysics*, vol. 175, no. 4, 2018. Also in ArXiv:1704.03552.
13. Korycansky, D. G.; and Lynett, P. J.: Offshore Breaking of Impact Tsunami: The Van Dorn Effect Revisited. *Geophysical Research Letters*, vol. 32, no. 10. URL `https://agupubs.onlinelibrary.wiley.com/doi/abs/10.1029/2004GL021918`.
14. Berger, M. J.; George, D. L.; LeVeque, R. J.; and Mandli, K. T.: The GeoClaw software for depth-averaged flows with adaptive refinement. *Advances in Water Resources*, vol. 34, no. 9, Sept. 2011, pp. 1195–1206. URL `http://www.sciencedirect.com/science/article/pii/S0309170811000480`.
15. LeVeque, R. J.; George, D. L.; and Berger, M. J.: Tsunami modelling with adaptively refined finite volume methods. *Acta Numerica*, vol. 20, May 2011, pp. 211 – 289.

REPORT DOCUMENTATION PAGE

Form Approved
OMB No. 0704–0188

1. REPORT DATE *(DD-MM-YYYY)* 01-03-2018	**2. REPORT TYPE** Contractor Report	**3. DATES COVERED** *(From - To)* 2016-2018

4. TITLE AND SUBTITLE
Modeling Issues in Asteroid-Generated Tsunamis

5a. CONTRACT NUMBER
NNA10DF26C

5b. GRANT NUMBER

5c. PROGRAM ELEMENT NUMBER

6. AUTHOR(S)
Marsha J. Berger and Randall J. LeVeque

5d. PROJECT NUMBER

5e. TASK NUMBER

5f. WORK UNIT NUMBER

7. PERFORMING ORGANIZATION NAME(S) AND ADDRESS(ES)
NASA Ames Research Center
Moffett Field, CA 94035

8. PERFORMING ORGANIZATION REPORT NUMBER
L–

9. SPONSORING/MONITORING AGENCY NAME(S) AND ADDRESS(ES)
National Aeronautics and Space Administration
Washington, DC 20546-0001

10. SPONSOR/MONITOR'S ACRONYM(S)
NASA

11. SPONSOR/MONITOR'S REPORT NUMBER(S)
NASA/CR–2018–219786

12. DISTRIBUTION/AVAILABILITY STATEMENT
Unclassified-Unlimited
Subject Category
Availability: NASA STI Program (757) 864-9658

13. SUPPLEMENTARY NOTES
An electronic version can be found at http://ntrs.nasa.gov.

14. ABSTRACT

This report studies tsunamis caused by asteroids, both those that arise from atmospheric blast waves moving across the water surface from airburst asteroids, and those that arise when the asteroid reaches the water and forms a crater. We perform numerical experiments that compare simulations using depth-averaged models (shallow water and several forms of Boussinesq) with linearized Euler (acoustics plus gravity) and ALE hydrocode simulations. We find that neither of the depth-averaged models do a good job of initiating the tsunami, but in some cases can be used to propagate a solution generated by a higher-fidelity method. A list of our conclusions and recommendations for further study is given in Section 5.

15. SUBJECT TERMS
tsunami, asteroid, airburst, crater, depth-averaged numerical simulations

16. SECURITY CLASSIFICATION OF:			**17. LIMITATION OF ABSTRACT**	**18. NUMBER OF PAGES**	**19a. NAME OF RESPONSIBLE PERSON**
a. REPORT	**b. ABSTRACT**	**c. THIS PAGE**			STI Information Desk (`help@sti.nasa.gov`)
U	U	U	UU	56	**19b. TELEPHONE NUMBER** ***(Include area code)*** (757) 864-9658

Standard Form 298 (Rev. 8/98)
Prescribed by ANSI Std. Z39.18